LJMU Research Online

Driver, SP, Robotham, ASG, Obreschkow, D, Peacock, JA, Baldry, IK, Bellstedt, S, Bland-Hawthorn, J, Brough, S, Cluver, ME, Holwerda, BW, Hopkins, A, Lagos, C, Liske, J, Loveday, J, Phillipps, S and Taylor, EN

 An empirical measurement of the Halo Mass Function from the combination of GAMA DR4, SDSS DR12, and REFLEX II data

http://researchonline.ljmu.ac.uk/id/eprint/16779/

Article

An empirical measurement of the halo mass function from the combination of GAMA DR4, SDSS DR12, and REFLEX II data

Simon P. Driver [ID],[1][*] Aaron S. G. Robotham [ID],[1] Danail Obreschkow [ID],[1] John A. Peacock [ID],[2]
Ivan K. Baldry [ID],[3] Sabine Bellstedt [ID],[1] Joss Bland-Hawthorn,[4] Sarah Brough [ID],[5] Michelle Cluver [ID],[6]
Benne W. Holwerda,[7] Andrew Hopkins,[8] Claudia Lagos,[1] Jochen Liske,[9] Jon Loveday [ID],[10]
Steven Phillipps [ID][11] and Edward N. Taylor[5]

[1]*International Centre for Radio Astronomy Research (ICRAR), University of Western Australia, Crawley, WA 6009, Australia*
[2]*Institute for Astronomy, University of Edinburgh, Royal Observatory, Edinburgh EH9 3HJ, UK*
[3]*Astrophysics Research Institute, Liverpool John Moores University, IC2, Liverpool Science Park, 146 Brownlow Hill, Liverpool L3 5RF, UK*
[4]*Sydney Astrophotonic Instrumentation Labs, School of Physics, The University of Sydney, Sydney, NSW 2006, Australia*
[5]*School of Physics, University of New South Wales, Sydney, NSW 2052, Australia*
[6]*Centre for Astrophysics and Supercomputing, Swinburne University of Technology, Hawthorn, VIC 3122, Australia*
[7]*Department of Physics and Astronomy, University of Louisville, 102 Natural Science Building, Louisville, KY 40292, USA*
[8]*Australian Astronomical Optics, Macquarie University, 105 Delhi Road, North Ryde, NSW 2113, Australia*
[9]*Hamburger Sternwarte, Universität Hamburg, Gojenbergsweg 112, D-21029 Hamburg, Germany*
[10]*Astronomy Centre, University of Sussex, Falmer, Brighton BN1 9QH, UK*
[11]*Astrophysics Group, School of Physics, Tyndall Avenue, University of Bristol, Bristol BS8 1TL, UK*

ABSTRACT

We construct the halo mass function (HMF) from the GAMA (Galaxy And Mass Assembly) galaxy group catalogue over the mass range of $10^{12.7}$–$10^{15.5}$ $M_\odot$, and find good agreement with the expectation from Lambda cold dark matter. In comparison to previous studies, this result extends the mass range over which the HMF has now been measured over by an order of magnitude. We combine the GAMA data release (DR) 4 HMF with similar data from the Sloan Digital Sky Survey (SDSS) DR12 and REFLEX II (*ROSAT*-ESO Flux Limited X-ray Galaxy Cluster Survey) surveys, and fit a four-parameter Murray–Robotham–Power function, valid at $\tilde{z} \approx 0.1$, yielding a density normalization of $\log_{10}(\phi_* \mathrm{Mpc}^3) = -3.96^{+0.55}_{-0.82}$, a high mass turnover of $\log_{10}(M_* M_\odot^{-1}) = 14.13^{+0.43}_{-0.40}$, a low-mass power-law slope of $\alpha = -1.68^{+0.21}_{-0.24}$, and a high-mass softening parameter of $\beta = 0.63^{+0.25}_{-0.11}$. If we fold in the constraint on Ω_M from the Planck 2018 cosmology, we are able to reduce these uncertainties further, but this relies on the assumption that the power-law trend can be extrapolated from $10^{12.7}$ $M_\odot$ to zero mass. Throughout, we highlight the effort needed to improve on our HMF measurement: improved halo mass estimates that *do not* rely on calibration to simulations; reduced halo mass uncertainties needed to mitigate the strong Eddington bias that arises from the steepness of the HMF low-mass slope; and deeper wider area spectroscopic surveys. To our halo mass limit of $10^{12.7}$ $M_\odot$, we are directly resolving ('seeing') 41 ± 5 per cent of the total mass density, i.e. $\Omega_{M,>12.7} = 0.128 \pm 0.016$, opening the door for the direct construction of three-dimensional dark matter mass maps at Mpc resolution.

Key words: surveys – galaxies: groups: general – galaxies: haloes – cosmological parameters – cosmology: observations – dark matter.

1 INTRODUCTION

One of the definitive predictions from the Lambda cold dark matter (ΛCDM) paradigm is the form (shape and amplitude) of the underlying dark matter halo mass function [HMF; see early works by Frenk et al. (1988) and Brainerd & Villumsen (1992) for example], and its evolution over time (see Reed et al. 2003; Lukić et al. 2007; Watson et al. 2013). The HMF describes the number density of dark matter haloes, either per mass interval or per log mass interval, with both forms in common usage. At redshift zero, the HMF can be described as a near-mass-divergent power-law distribution, with a high-mass cut-off correlated with the mass assembly time since the big bang.

The HMF form can be derived heuristically from the Press–Schechter theory for the gravitational collapse of overdense condensates (Press & Schechter 1974). The theory of the HMF was subsequently placed on a sounder basis via the random-trajectories approach, which allowed an understanding of the fate of material in underdense regions and a solution of the 'cloud-in-cloud' problem (Peacock & Heavens 1990; Bond et al. 1991).

The initial HMF, established at the time of decoupling, then evolves through the process of hierarchical assembly of smaller dark matter haloes. This results in an HMF with both a time- and scale-
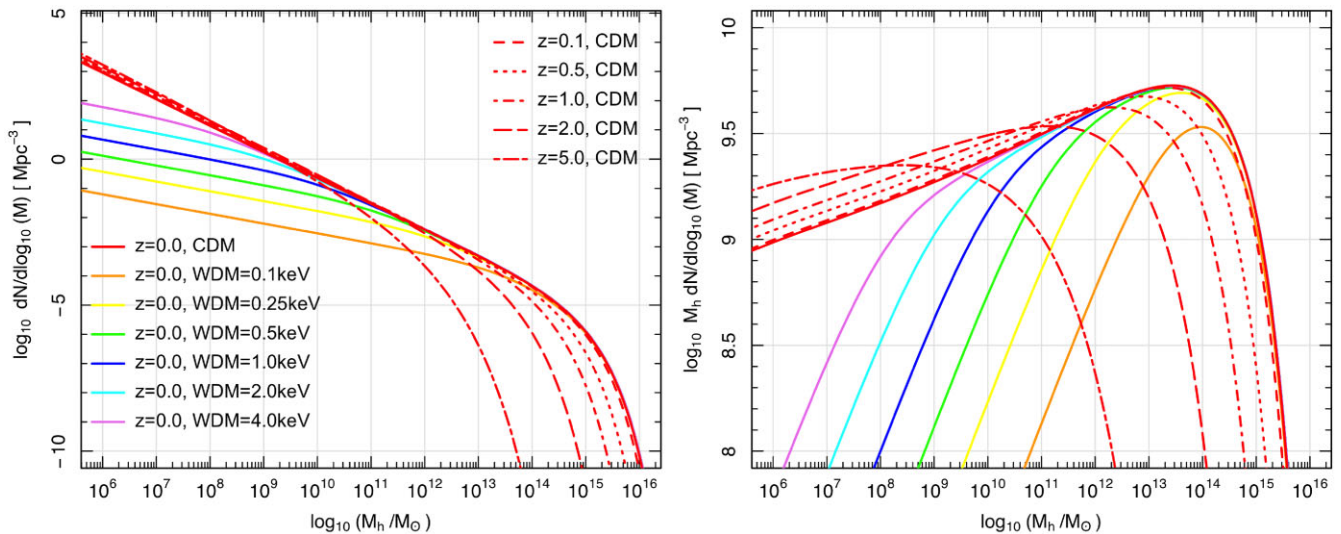
Figure 1. (Left) Analytical predictions of the HMF over a very broad halo mass range (lines), its predicted evolution with redshift (red lines), and its dependence on the dark matter particle mass (coloured lines). (Right) The same predictions as the left-hand panel, but now showing the contribution of each decade of halo mass to the total matter density, and highlighting the mass range where most mass is predicted to reside. All the curves shown are taken from Murray et al. (2013); see also Murray et al. (2021) for a recent revision and online tool.

invariant power law at masses below some time-dependent cut-off mass (see e.g. Jenkins et al. 2001; Reed et al. 2007). The HMF also emerges naturally from numerical simulations of the evolving dark matter distribution, albeit with a 10–20 per cent variation within a particular simulation (Ondaro-Mallea et al. 2021) and a 10–20 per cent variation between simulations (Murray, Power & Robotham 2013).

Recently, Murray, Robotham & Power (2018) demonstrated that the HMF can be described by a four-parameter function (hereafter, the MRP function; see equation 3) to within 5 per cent accuracy at any mass interval. The MRP function closely relates to the Schechter function (Schechter 1976), which is commonly used for fitting galaxy luminosity and/or stellar mass functions (e.g. Driver et al. 2022) and which can be derived from the Press–Schechter formalism. The one difference between the MRP and Schechter functions is the addition of a parameter (β) to soften or sharpen the exponential cut-off at high mass.

This exponential cut-off at the high-mass end of the HMF is expected to evolve significantly (Reed et al. 2003; see red lines in Fig. 1), as progressively larger haloes form over time from the hierarchical merging of the dark matter haloes. This results in the emergence of massive dark matter haloes ($\geq 10^{14.5}\,M_\odot$) hosting rich clusters of galaxies around a redshift of unity (Allen, Evrard & Mantz 2011). Hence, the existence and evolving density of high-redshift high-mass clusters is a key and stringent test of ΛCDM (Allen et al. 2011; Asencio, Banik & Kroupa 2021).

The dark matter particle mass can also influence the low-mass end of the HMF, as illustrated in Fig. 1, with any low-mass cut-off directly linked to the dark matter particle mass for some early-decoupling weakly interacting massive particle (e.g. Murray et al. 2013). For ΛCDM, this mass cut-off is around Earth mass, but in warm or hot (neutrino) dark matter it can be as high as $10^{13}\,M_\odot$ for dark matter particles of around 0.1 keV (see Fig. 1). This is due to the propensity of hot or warm dark matter to free stream during the era in which the particles are relativistic. If the dark matter consists of a very heavy particle (> many keV), or even primordial black holes (0.5–$100\,M_\odot$), then no detectable low-mass cut-off would be expected.

The HMF is hence a critical probe of ΛCDM, with at least three distinct testable facets:

(i) the high-mass cut-off and its evolution with redshift;
(ii) the power-law slope and amplitude of the HMF; and
(iii) the existence and location of any low-mass cut-off or perceived flattening in the low-mass slope.

A slightly more subtle test is the first moment of the HMF, the integration over all masses (see the right-hand panel of Fig. 1), which should be consistent with the total matter density. For completely cold dark matter, all dark matter particles should be accounted for when summing over haloes down to infinitesimal mass; however, in the case of Warm Dark Matter (WDM) or Hot Dark Matter (HDM), the effects of free streaming mean that there will be a subset of mass that is not associated with haloes, so that the integral of the local HMF may lie below the density inferred at recombination by cosmic microwave background (CMB) studies. Fig. 1 illustrates these two tests and hence the importance of measuring the HMF. Fig. 1 (right-hand panel) highlights how the majority of matter is predicted to reside in intermediate- to low-mass haloes (i.e. ~60 per cent in the range of $10^{14.5}$–$10^{11}\,M_\odot$), hence demonstrating the importance of establishing group catalogues to low halo masses.

On the observational side, the measurement of the HMF appears tractable and relatively straightforward (see Bahcall & Cen 1993), but does hinge critically on group/cluster identification, and especially on robust halo mass estimates from group/cluster sizes and velocity dispersions. In general, the observational and analysis pathway is a simple task: construct a group catalogue, estimate masses, and convert to a volume-limited space density. Comparison of the observed and predicted HMF can be made in multiple redshift slices and over as broad a mass range as the observations permit. Typically, this direct approach has been pursued in two ways: (i) via X-ray detection of galaxy clusters (e.g. Böhringer, Chon & Fukugita 2017) and (ii) via group finding within large spectroscopic surveys (e.g. Eke et al. 2004). Both Böhringer et al. (2017) and Eke et al. (2006) show good agreement (~10–20 per cent), with the HMF predicted by ΛCDM over the halo mass range of $10^{13.75}$–$10^{15.25}\,M_\odot$, but also have

significant subtleties, not least of which is a reliance on numerical simulations of the matter (and plasma for the X-ray pathway) to calibrate the mass estimates.

In the former, one has to rely on the correct calibration of the L_X–M relation (Stanek et al. 2006; Hoekstra et al. 2011), or rather the better understood L_X–T relation, and any variation with redshift (Leauthaud et al. 2010). One also has to worry about virialization, variance in the plasma properties (temperature especially in what may well be a mixed multiphase medium), and the general bias towards selecting denser and higher L_X clusters, given that detection is inevitably subject to some X-ray flux and flux contrast limit. The final amplitude of the predicted HMF is also dependent on the underlying clustering strength, with lower σ_8 values giving rise to higher than expected numbers of rich clusters. Moreover, as the X-ray flux of intermediate-mass groups is minimal, either because the plasma is much cooler or not present, this method may only be viable at moderate to high group/cluster masses (i.e. $M \geq 10^{13} \, M_\odot$), hence not capable of probing to lower halo masses (i.e. ∼30 per cent of the total predicted dark matter content). Progress in this area may be possible through the stacking of X-ray data at the locations of known galaxy groups: see the promising results from using Sloan Digital Sky Survey (SDSS)-selected galaxy samples to stack the *ROSAT* data by Anderson et al. (2015) (see also more general discussion on this topic in Driver 2021) or via stacking at millimetre wavelengths via the Sunyaev–Zeldovich effect (Singari, Ghosh & Khatri 2020).

For the large wide-area spectroscopic surveys, e.g. two-degree field galaxy redshift survey (2dFGRS; Colless et al. 2001), SDSS (York et al. 2000), GAMA (Galaxy And Mass Assembly; Driver et al. 2009, 2011), DEVILS (Davies et al. 2018), WAVES (Driver et al. 2016, 2019), DESI (Dey et al. 2019), etc., one has to worry about spectroscopic completeness that biases against lower mass groups with fewer members, biases in the group-finding algorithm (missed groups and/or false positives), and the inherent uncertainties in converting the measured redshifts into velocity dispersions and robust halo masses. The latter aspect becomes especially hard when the multiplicity, i.e. the number of group members, is only a few.

These problems, inherent in both the X-ray and spectroscopic survey approaches, are tractable but the results are susceptible to strong biases, some of which arise from the large random uncertainties. Paramount among these is the Eddington bias that emerges from the uncertainty in the halo masses, and whose impact is exacerbated by the steepness of the HMF (see Fig. 1). Hence, a significant systematic mass shift can arise as the haloes are scattered to higher or lower masses during the measurement process.

One further aspect worth considering is the practice of calibrating the group-finding algorithms to numerical simulations, i.e. linking lengths, and the mass scaling factor (A). This calibration process fundamentally links the empirical results to a specific semi-analytical model built upon an underlying dark matter simulation (see Eke et al. 2004; Robotham et al. 2011). We note that the recent analysis of Tempel et al. (2014) attempts to avoid this issue by calibrating the tangential linking length to the mean observed galaxy separation within redshift slices. Even more concerning are techniques that involve abundance matching, in which halo masses are assigned based on some rank order, and where the recovered HMF, by construction, is required to match that of the adopted simulation (see the review by Wechsler & Tinker 2018).

A more statistical approach to probing the HMF comes from weak lensing studies (see e.g. Viola et al. 2015; Dong et al. 2019; Rana et al. 2022), in which an adopted HMF combined with assumptions of the DM profiles can be used to predict the lensing signature and

compared to that measured. This method too has issues, mainly the need for a calibration, or adoption, of a specific HMF form and a universal DM profile shape that is poorly constrained especially at intermediate halo masses. It also has the disadvantage of not providing mass on a halo-by-halo basis, but the significant advantage of not needing to provide mass on a halo-by-halo basis, mitigating the concern over the Eddington bias.

Finally, a viable alternative to measuring and comparing the HMF is to measure and compare the line-of-sight velocity dispersions with the three-dimensional (3D) velocity dispersions from simulations. This approach bypasses the additional uncertainties around halo mass estimation (see e.g. Caldwell et al. 2016), but is not without its own issues given the often limited number of velocity dispersion measurements for each halo. However, perhaps a stronger reason for pursuing the halo mass measurement pathway is that fundamentally we are interested in the determination of masses on a halo-by-halo basis, partly to not only study the variations of galaxy properties (and evolutionary pathways) as a function of halo mass, but also to investigate how Ω_M, as constrained by cosmological measurements, is broken down into discrete self-gravitating clumps.

Current and future spectroscopic surveys have, in varying degrees, built their science cases around the measurement of both halo masses and the HMF (GAMA, Driver et al. 2011; WAVES, Driver et al. 2016, 2019; DEVILS, Davies et al. 2018), and while in practice the pathway looks straightforward the reality has proved more elusive.

Here, we attempt to construct an HMF from the GAMA survey and in this work look to follow an *empirical* pathway, while articulating the difficulties in doing so. Where possible, we explore the dependence of our fitted HMF MRP parameters on some of the issues raised above, and compare our HMF to the few existing published measurements, which include 2PIGG (Eke et al. 2006), SDSS (Tempel et al. 2014), and REFLEX II (*ROSAT*-ESO Flux Limited X-ray Galaxy Cluster Survey; Böhringer et al. 2017). We later combine these data to provide a joint constraint on the MRP HMF parameters, and compare to the prediction from ΛCDM. Throughout, we attempt to highlight key issues that need to be addressed to produce precision HMF measurements as new surveys that warrant such robustness come online (e.g. DESI and WAVES). Future papers will address biases in more detail, and seek to improve further on our halo mass estimates and more robust errors, as well as using bespoke simulations to better understand the systematics that emerge through the group-finding process and its calibration.

In Section 2, we describe the GAMA group catalogue (G^3C), the mass measurements, and the mass errors. In Section 3, we describe our methodology for constructing the GAMA HMF, and show our attempts to fit the MRP function. In Section 4, we combine the GAMA data with that from the SDSS, 2PIGG, and REFLEX II data sets, to provide a final joint HMF constraint, and discuss some of the broader and ultimately more speculative implications.

We use the Planck 2018 cosmology throughout, namely $\Omega_M = 0.3147 \pm 0.0074$, $\Omega_\Lambda = 1 - \Omega_M$, and $H_0 = 67.37 \pm 0.54 \, \mathrm{km \, s^{-1} Mpc^{-1}}$ (Planck Collaboration VI 2020, table 1, col. 6 – combined). For comparison with studies that use other cosmologies (especially the common units with explicit powers of h), our numbers should be scaled as follows:

Halo masses:

$M \propto H_0^{-1}$; i.e. our units are $M_\odot \, h_{P18}^{-1}$.

Space densities:

$\phi \propto H_0^3$; i.e. our units are $\mathrm{Mpc^{-3}} \, h_{P18}^3$,

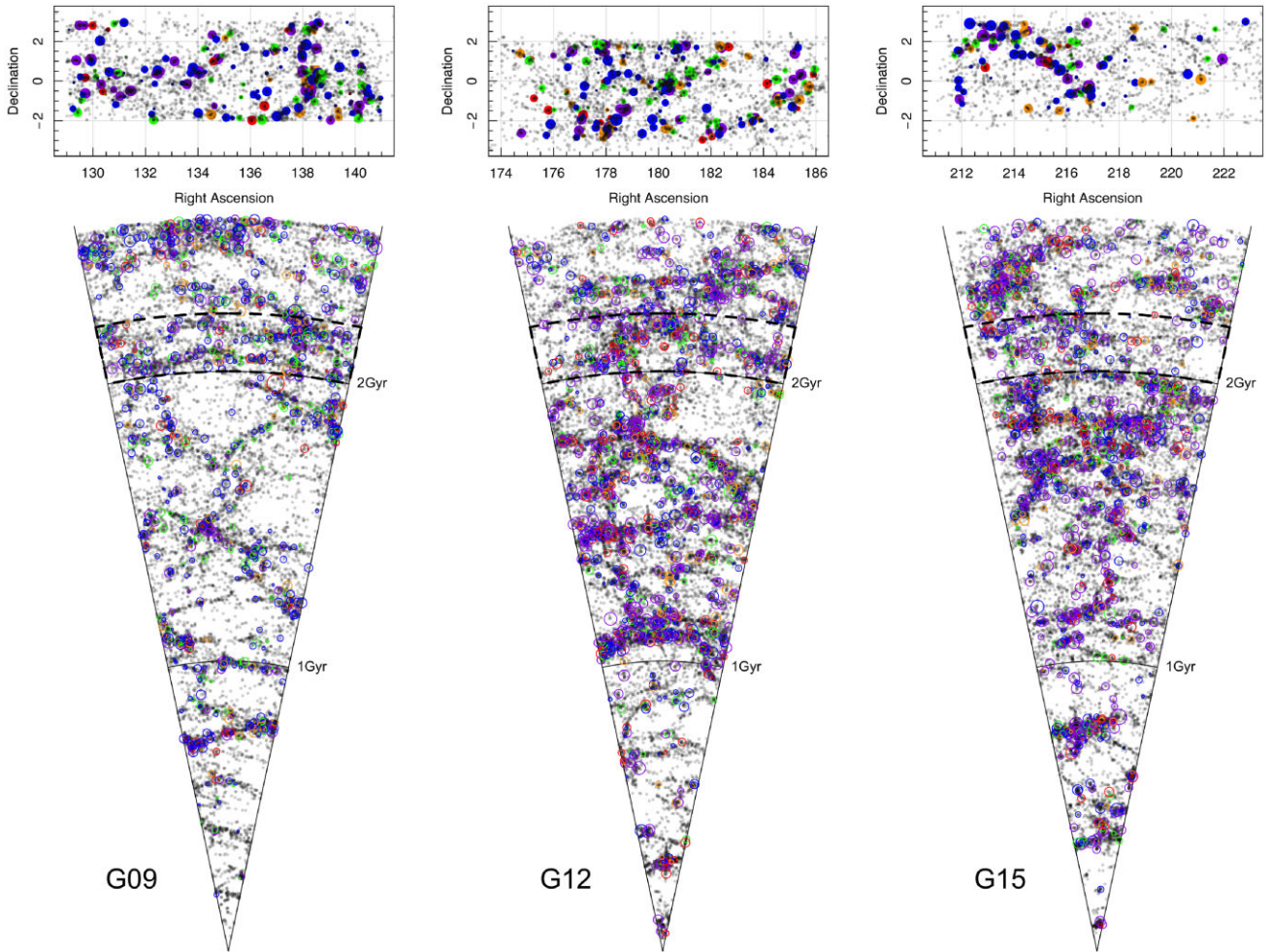where $h_{P18} = H_0/(67.37 \, \mathrm{km \, s^{-1} \, Mpc^{-1}})$.

Figure 2. Each panel shows a cone plot of the GAMA group (coloured circles) and galaxy (grey dots) distributions to a maximum redshift of 0.3, indicating lookback time (lower cones), and in (upper panels) right ascension and declination for a narrow redshift slice indicated by the dashed rectangles in the lower panels. The group circles are coloured according to multiplicity, with 'blue', 'green', 'orange', 'red', and 'purple' denoting multiplicities (N_{FoF}) of 3, 4, 5, 6, and >6, respectively. Circle sizes are scaled according to $\log_{10}(M_{FoF})$.

2 THE GAMA GALAXY GROUP CATALOGUE (G^3C)

The GAMA survey (see Driver et al. 2011, submitted; Liske et al. 2015) has provided over 300 000 spectroscopic redshifts from the Anglo Australian Telescope's AAOmega facility, combined with pre-existing literature measurements. The GAMA survey covers 250 square deg of sky in five distinct regions (G02, G09, G12, G15, and G23), and the three primary equatorial regions (G09 + G12 + G15) cover 179.92 square deg. Within these equatorial regions, GAMA achieved over 98 per cent redshift completeness (see Liske et al. 2015), to the flux limit of $r_{SDSS} = 19.8$ mag.

Using a friends-of-friends algorithm, calibrated to the GALFORM semi-analytic model (Bower et al. 2006) built on to the Millennium dark matter simulation (Springel et al. 2005), Robotham et al. (2011) constructed the G^3C. The reliance of the catalogue on the simulations will be discussed at various stages below, but the final G^3C catalogue consists of 26 194 galaxy groups and pairs, of which 9718 groups have a multiplicity of 3 or greater, and 3061 with a multiplicity of 5 or more. The catalogue identifies more massive groups to $z > 0.4$, but for the present analysis we impose an upper limit of $z = 0.25$ in order to reduce complications from evolution of the HMF and also redshift-dependent systematics in mass estimation. This cut

yields 5241 groups with a multiplicity ≥3 and 1732 groups with a multiplicity ≥5. The mean redshift of the latter subset is 0.153.

Fig. 2 shows the spatial distribution of the group catalogue for multiplicity ≥5 systems. Each of the three equatorial GAMA regions is shown independently, with the top panels showing the right ascension and declination distribution for a narrow redshift slice, while the lower panels show the light-cones in lookback time and where the dashed line indicates the selected redshift slice. Symbol sizes are linked to $\log_{10} M_{FoF}$, and the underlying grey data points show the full GAMA spectroscopic catalogue. Symbol colours denote multiplicity (see the caption). The large-scale structure, which traces the underlying dark matter distribution, is clearly evident, as is the known general underdensity of the G09 region. Fly-through animations of these cones are available from the GAMA data release (DR) 4 website.[1]

2.1 G^3C velocity dispersion and total mass estimates

Total masses for the G^3C sample were estimated from the velocity dispersion (σ), which in turn were derived from the group member

---

[1]http://www.gama-survey.org/dr4

CMB frame redshifts using the GAPPER estimator (see Beers et al. 1990). This estimator includes consideration of: the magnitude distribution of the objects contributing to the velocity dispersion; the redshift of the cluster/group equalling that of the brightest member; and the mean uncertainty in the redshifts from our intrinsic redshift measurement error of $\pm 50 \, \mathrm{km \, s^{-1}}$ (Baldry et al. 2014; Liske et al. 2015). For full details as to how the G^3C velocity dispersions are derived, see equations (16) and (17) from Robotham et al. (2011).

The total dynamical masses (M_{FoF}) are then determined, assuming fully virialized haloes, via

$$M_{\mathrm{FoF}} = \frac{A}{G} \sigma^2 R_{50}, \tag{1}$$

where A is some normalizing factor (typically ~ 10), G is the gravitational constant, σ is the line-of-sight velocity dispersion, and R_{50} is the projected radius containing 50 per cent of the group members (see section 4.2 of Robotham et al. 2011, for a discussion concerning the optimal radius). In a virial equation such as equation (1), one would normally write R_{50} in proper units – but we choose to use comoving units, so that all lengths in this paper are comoving (although velocities are in physical units). The same choice was made by Robotham et al. (2011), and it had no impact on the results of that paper because the scaling factor was calibrated as a function of redshift and richness using simulations: thus, any change in $A(z)$ from moving between proper and comoving lengths is automatically accounted for. The values of A for the present updated catalogue were determined similarly, by running the same group finder and mass estimation algorithm on nine equivalent-volume mock catalogues (see Merson et al. 2013) with identical properties to GAMA (i.e. volumes, magnitude limits, redshift errors, and incompleteness). This aspect is discussed further in Section 2.3.3.

The values for A were found to range from 10.7 to 19.2 depending on group multiplicity, redshift, and the adopted magnitude limits. Hence, the mass value, MASSAFUNC, in the G^3C catalogue (G3CFoFGROUPV10) uses an optimized A value for each group, based on its redshift and multiplicity, whereas the MASSA masses simply use the formula shown in equation (1) with comoving R_{50} values and a constant value of $A = 10$.

While the MASSAFUNC values are designed to be as correct as possible in a ΛCDM universe, there may be some concern about excessive reliance on inexact simulations. We therefore also consider the simpler and less fine-tuned alternative of adopting a single typical value of A. The mean ratio between MASSAFUNC and MASSA for groups within our nominal limits ($z < 0.25$ and $M > 10^{13} \, \mathrm{M_\odot}$) is $M_A/M_{\mathrm{Afunc}} = 0.72$, and hence we will adopt $A = 13.9$ as the best choice for the case of fixed A. We make the resulting mass estimates our primary choice for the HMF analysis, although we also report results based on the full MASSAFUNC estimates.

The robustness of the G^3C halo masses has been independently confirmed through comparison with weak lensing constraints from the ESO VLT Survey Telescope's Kilo Degree Survey (see Viola et al. 2015). Their equation (38) shows good consistency between KiDS and GAMA (equation 1), in the mass normalization (1.00 ± 0.15) around $10^{14} \, \mathrm{M_\odot}$, with an average scatter (i.e. mass error) of $\sigma_{\log_{10} M} \sim 0.20$. However, the weak lensing does find evidence for non-isothermal behaviour of the mass profiles and this is discussed further in Section 2.3.1.

Chauhan et al. (2021) also tested the Robotham et al. (2011) mass estimates against an independent semi-analytical model, SHARK (Lagos et al. 2018), showing that the inferred M_{FoF} were in good agreement with the intrinsic halo masses of the model for groups containing ≥ 5 members. Hence, we will adopt $N_{\mathrm{FoF}} \geq 5$ for our

baseline HMF measurement but also show results for a range of N_{FoF} cuts.

2.2 G^3 mass error estimates

Individual mass errors for each halo are not provided within the G^3C catalogue, although the weak lensing results do provide an indication of the average mass error. Here, we derive an approximate mass error as a function of group multiplicity, by identifying those groups with more than 20 members, and for which the mass estimates should be stable and reliable. This constitutes 154 groups and for each of these groups we gradually remove group members, by removing the system with the faintest flux, and recomputing the group's σ and R_{50} values, and via equation (1) (with $A = 13.9$) the halo mass.

Fig. 3 shows as blue green lines a trail for each of the 154 groups (with $N_{\mathrm{FoF}} > 20$). These trace out the recovered-to-original mass ratio, i.e. $\log_{10} (M_N/M_{\mathrm{max}})$, as the multiplicity decreases. The solid red line shows the median of these trails, while the dashed red lines show the limits that enclose 84 (upper line) or 16 (lower line) per cent of the trails. These lines suggest a very small error at high multiplicity, which grows significantly as the multiplicity is reduced. The trails are colour coded by mass, as labelled, and no obvious trend with mass is seen.

The dashed black horizontal lines represent the global mass uncertainty seen by Viola et al. (2015) and are consistent with the mean/median multiplicity of our sample of $N = 7.6/5.0$. The dotted black lines are a transcription of the error estimate shown in fig. 8 from Robotham et al. (2011) and also defined by their equation (20); these imply significantly greater uncertainty. The difference between our estimate and those provided in Robotham et al. (2011) is unclear, but we note that our results are consistent with a recent analysis by Meyer (2021; UWA Master's thesis), who explored the robustness of G^3C masses based on extensive numerical simulations. We therefore adopt the mass uncertainty based on the sum in quadrature of our multiplicity implied error and an error floor of $\sigma_{\log_{10} M} = 0.10$ (motivated by the work of Meyer 2021). We also implement, for our MASSA values only, the correction implied by the median (solid red line from Fig. 3), which suggests some bias towards lower masses at very low multiplicities (i.e. $\Delta \log_{10} M \sim 0.1$ at $N_{\mathrm{FoF}} \sim 6$).

Fig. 3 raises an interesting question, as given the significance of the mass error, its uncertainty, and the susceptibility to a severe Eddington bias, it is not clear whether a more reliable HMF is built by including low-multiplicity systems to maximize the sample size or by selecting a smaller high-multiplicity high-fidelity sample. To address this, we will explore a range of multiplicity cuts when generating the GAMA HMF in Section 3 and adopt $N_{\mathrm{FoF}} \geq 5$ as our primary cut given the significant increase in uncertainty at $N_{\mathrm{FoF}} < 5$.

2.3 Some digressions

Before moving on to derive the GAMA HMF, it is worth highlighting a number of issues in the construction of the group catalogue to maximize transparency and motivate future work.

2.3.1 The mass estimation formula

The functional form shown in equation (1) resembles that of a singular isothermal sphere, where the mass within a radius R is $M = 2\sigma^2 R/G$ (see e.g. Binney & Tremaine 2008). A divergent mass is generally circumvented by using a truncated isothermal sphere
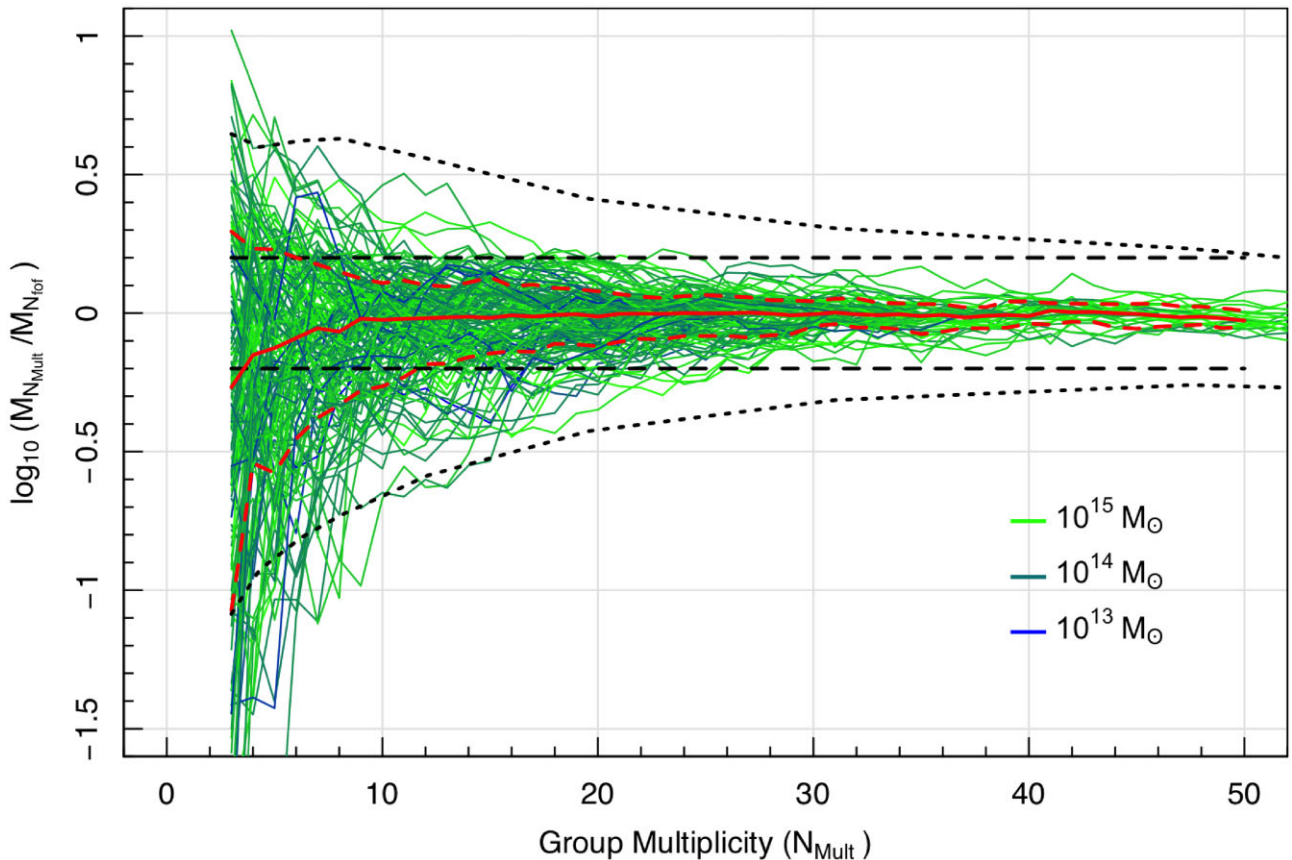
Figure 3. The determination of our mass error as a function of multiplicity. For all GAMA groups with more than 20 members, we calculate the change in the mass as the multiplicity decreases (blue green coloured lines). The trail colour indicates the original halo mass (see the key). In red are the 16, 50, and 84 per cent quantiles. The dotted black lines show the initial error estimate from Robotham et al. (2011), while the dashed black lines show the mean weak lensing error estimate from Viola et al. (2015).

model (see e.g. Brainerd et al. 1996; Brimioulle et al. 2013), which relies on introducing some limiting radius. This is typically taken as the r_{200} value, which represents the radius within which the average density is 200× the critical density. In this case, we expect the total mass to scale $\propto R^3$, so that $M \propto \sigma^3$. Any radius can be used in combination with an appropriate $[A, R]$ pairing; see equation (1). However, generally some uncertain extrapolation is required from the mass within the half-light radius (which can generally be measured robustly: see Strigari et al. 2007) to the total mass.

Ultimately, the value of A and the choice of R are critical, and can act to shift the entire HMF to higher or lower masses. The presence of substructure can also bias masses high if not accounted for (see e.g. Tempel et al. 2017; Old et al. 2018; Tucker et al. 2020).

Two lensing studies have looked to verify the G^3C masses (Han et al. 2015; Viola et al. 2015), and find consistency in the mean mass at around $10^{14} \, M_\odot$, but a shallower trend with σ of $M \propto \sigma^2$ (so two-thirds of the expected slope). This shallower σ dependence would predict no groups/clusters above a mass of $10^{14.7} \, M_\odot$, which is contrary to observational constraints (e.g. the Coma cluster, Sohn et al. 2017; or El Gordo, Jee et al. 2014; Asencio et al. 2014). It is hard to know how much of a concern this is for this work, since the slope of the M–σ relation is hard to measure accurately given the few extremely massive objects in the GAMA samples used for lensing studies. We can take some reassurance from the fact that the weak lensing masses scale very nearly linearly with total r-band group luminosity, and this alternative mass proxy correlates very well with our dynamical estimates.

Nevertheless, it would be desirable to improve the absolute calibration of group mass estimates, preferably in a way that is independent of simulations. A radical proposal by Caldwell et al. (2016) is that we should move away from mass comparisons entirely, and compare velocity dispersion distributions instead. This idea clearly has some merit as it dispenses with the need for a scaling parameter, i.e. A. This would, however, require careful consideration of line-of-sight velocities versus 3D velocities, which is non-trivial (see Elahi et al. 2018).

2.3.2 The value of the mass calibration scaling value, A

By adopting a constant value of $A = 13.9$ for our MASSA values, we lessen our detailed reliance on simulations for mass calibration. Ultimately, this parameter can be probed empirically, via logic that goes back to Zwicky (1933) and his attempt to reconcile the measured velocity dispersion of Coma ($\approx 1000 \, \mathrm{km \, s^{-1}}$) with that predicted by its visible mass alone of $80 \, \mathrm{km \, s^{-1}}$. Zwicky's derivation of A was based on the virial theorem, coupled with the assumption of an isothermal mass distribution, and where he found $A = 1.667$ (Zwicky 1933), and that appeared to underpredict the mass content by a factor of 400.

Since Zwicky (1933), our measurements of Coma have improved substantially, including direct measurements of the total dynamical mass. A robust total mass of $M_{200} = 1.88^{+0.65}_{-0.56} \times 10^{15} \, h^{-1} \, M_\odot$ within an r_{200} radius of $1.99^{+0.21}_{-0.22} \, h^{-1} \, \mathrm{Mpc}$ has been derived from gravita-

tional lensing (Kubo et al. 2007). This mass and size are on the whole consistent with a range of earlier estimates stretching from 0.8 to $1.9 \times 10^{15}\,h^{-1}\,\mathrm{M}_\odot$. As Coma's line-of-sight velocity dispersion is $947 \pm 31\,\mathrm{km\,s^{-1}}$ (Sohn et al. 2017), and the projected half-light radius is $R_{50} = 1.4\,h^{-1}\,\mathrm{Mpc}$ (Doi et al. 1995), this implies a value of $A \approx 6 \pm 3$ that is less than half of our adopted value of $A = 13.9$. More precision and clarity over A are clearly required, and hopefully as detailed studies of more clusters emerge one will eventually be able to obtain a fully simulation-independent estimate of A and its dependence on halo mass and other variables.

2.3.3 Comoving distance or proper (angular diameter) distance

As discussed earlier, we have chosen to base our mass estimate on the comoving sizes of clusters, rather than using the angular diameter distance to derive physical radii. This follows the convention established by Eke et al. (2004) and Robotham et al. (2011), but over a wide range of redshifts it might be considered problematic. If the virial relation applied rigorously in proper coordinates, then the use of comoving half-light radii would require a scaling $A(z) \propto 1/(1+z)$. This is not a concern for the current work, for a number of reasons. First, the redshifts probed are relatively local ($z < 0.25$), so that there is no real ability to probe evolution, and we are interested only in A at a single effective redshift. Furthermore, the redshift-dependent group selection effects complicate any simple virial relation, meaning that it is better to work empirically rather than enforce a simplistic virial relation.

However, this issue will be important in future deeper studies that probe to significant redshifts. We can anticipate an increase in the frequency of non- or partially virialized haloes as our surveys advance to higher redshifts, and also as we probe to lower masses where the systems may exhibit more structure (i.e. be less dynamically relaxed).

Note that by fitting for $A(z)$ one effectively folds in this dependence on A; however by opting for a fixed A we have removed this dependence, perhaps reopening the issue as to which distance one should use. As our R_{50} values are inevitably well within the r_{200} radii, and very much within the bound region, the case for using the angular diameter distance starts to looks stronger. Later, we will report results from both but continue to adopt the convention defined by Eke et al. (2004) and Robotham et al. (2011).

2.3.4 Linking lengths and overdensities

Critical to the operation of the group-finding friends-of-friends algorithm are the linking lengths in the spatial and redshift directions (see e.g. Duarte & Mamon 2014). These define whether a galaxy is or is not a member of a group. The linking lengths are derived by testing against a mock catalogue, and modifying the lengths until one recovers the known haloes. This is typically done in a bijective manner (Robotham et al. 2011), i.e. a false positive carries the same penalty as a missing group or cluster, and one looks to find the optimal lengths that minimize both.

At high mass, linking-length uncertainties are a relatively weak concern, as the interloper density is relatively low. Increasing the linking lengths has a fairly minimal impact at high masses and high multiplicities, although it can lead to the merging of nearby groups into superclusters.

At low mass, the addition of a single bogus member, or loss of a real member, can introduce significant mass errors. Further investigation is needed to explore this dependence in detail, and it is left for future work.

One possible advancement will be to fold in the expected group profile shape into the friends-of-friends search algorithm, essentially moving towards halo finding as used in numerical simulations (for a summary of halo finders, see Knebe et al. 2013, and for an initial attempt in this direction see Tempel et al. 2018). In due course, it will be important to build complete end-to-end Monte Carlo simulations that model the reliance that includes the linking-length uncertainty.

In all of this, we should bear in mind that there is an ambiguity in defining the 'true' masses. We have calibrated to M_{200}, which is the mass within the r_{200} radius. These values ultimately depend, by their definition, on the critical density. An alternative convention is to define r_{200} as the radius within which the mean density is 200 times the *background* value (only 63 times the critical density for our fiducial cosmology). Defining M_{200} via the background density would shift the HMF to higher masses. This shift can be estimated using NFW halo profiles (Navarro, Frenk & White 1997): For a typical NFW concentration of 5, the mass defined at 200 times the background is 1.4 times the mass at 200 times critical, and this correction factor is rather insensitive to mass. Since N-body halo catalogues are computed using algorithms similar to FoF, which scale with the mean particle density, it could be argued that defining M_{200} with respect to the background would be a more consistent approach. However, we continue to use the definition with respect to the critical density, for consistency with the literature on gravitational lensing.

3 THE GAMA HMF

The G^3C catalogue contains mass estimates down to $10^{10}\,\mathrm{M}_\odot$ and extends out to $z \approx 0.6$; however, masses below $10^{12}\,\mathrm{M}_\odot$ become increasingly unreliable, due to low multiplicity, irregularity, and the propensity to be impacted more significantly by an interloper. We hence confine ourselves to $z < 0.25$ where the number of multiplicity ≥ 3 groups is $N_g = 5246$. As discussed later, we will construct multiple HMFs with various N_{FoF} selections, and show figures in the main text based on the results from $N_{\mathrm{FoF}} \geq 5$ but with all results reported in the tables, and all derived HMFs shown in the appendices. Ultimately, $N_{\mathrm{FoF}} \geq 5$ represents a trade-off between sample size and fidelity in our measurements, while the redshift limit ensures that any evolution of the HMF will have a negligible impact on our measurements.

For clarity, we first provide a summary of the method we implement, and where Fig. 4 shows the resulting HMF:

(i) Construct the raw HMF (halo density per log mass interval), using a $1/V_{\mathrm{max}}$ estimator, where V_{max} of the group is based on the limiting z of the nth group member.

(ii) Run a Monte Carlo of the following (1001 $\times$):

    (a) Perturb each group's mass by its mass uncertainty assuming a lognormal error distribution.

    (b) Re-derive the HMF using the same $1/V_{\mathrm{max}}$ estimates.

(iii) Determine the mean of the revised density estimated in each mass interval, and the 16/84 per cent quantiles from the Monte Carlo simulations.

(iv) Determine the multiplicative offset between the original HMF and the median Monte Carlo HMF for each mass interval.

(v) Reduce the original HMF values by this multiplier to produce the final HMF (thereby correcting for the Eddington bias inherent in the original measurement).

(vi) Assign the quantile error in each mass interval from the Monte Carlo simulation as the Eddington bias correction error.
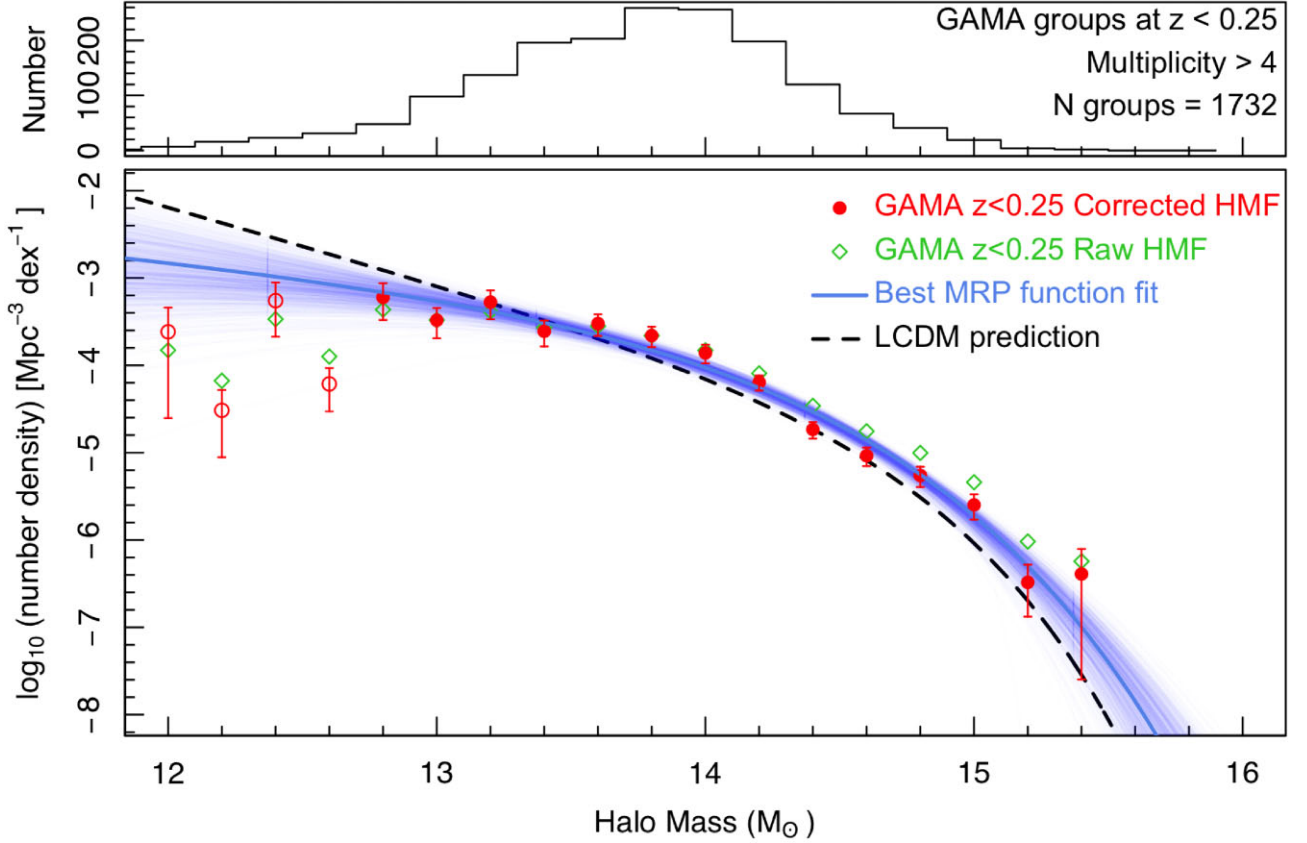
Figure 4. (Upper) The original histogram of the number of GAMA groups at $z < 0.25$. (main panel). The recovered HMF before (green arrows) and after (red points) the Eddington bias correction. The black dashed line shows the expected MRP function from Murray et al. ([2021](#)), while the blue line shows the best MRP function fit and the fainter blue lines are from the Monte Carlo realizations. Solid symbols denote where the data are complete and hence to which the MRP function is fitted, and the open symbol the onset of incompleteness. The dashed line shows the ΛCDM prediction for our fiducial cosmology, evaluated at the effective redshift $z_{\rm eff} = 0.1$.

(vii) Determine the Poisson and Cosmic Variance errors for the original distribution assuming root-n statistics and the CV formula from Driver et al. ([2011](#)).

(viii) Combine the Eddington bias uncertainty and the Poisson error in quadrature to obtain the total error on the final HMF.

In Section [3.1](#), we elaborate on this summary, to provide additional details and highlight some of the subtleties, in Section [3.2](#) we describe our MRP function, our fitting process and fitting errors, and in the remaining sections some further digressions.

3.1 Determination of the GAMA HMF

We construct the GAMA HMF via a standard $1/V_{\rm max}$ method, modified to operate on groups, i.e.

$$\phi(\log_{10}[M/M_\odot]) = \sum_{i=0}^{N_{\rm group}} \left(\frac{w_i}{V_{\rm max}^i \Delta \log_{10} M} \right), \qquad (2)$$

where $V_{\rm max}^i$ is the maximum comoving volume over which the ith group can be detected, w_i is the multiplicative Eddington bias correction for that mass interval (discussed later), $\Delta \log_{10} M$ is the bin width, and $N_{\rm group}$ is the total number of groups. The $V_{\rm max}$ values represent the distance at which the nth brightest group member is no longer detectable, and where n is the selected multiplicity limit for acceptance as a group. These $V_{\rm max}$ (or rather $z_{\rm max}$) values for each

individual galaxy are reported in the STELLARMASSESV19 DMU as Z19PT8.

In practice, for each group we identify the members of the group, using G3CGALS within the GroupFinding DMU, and rank them by apparent r-band flux. We match this catalogue to the STELLARMASSESV19 catalogue, and adopt the redshift limit of the nth member. For any group whose redshift exceeds its nth galaxy redshift limit, we reset the limit to its current redshift and for any group whose $z_{\rm max}$ exceeds our redshift boundary we reset it to $z_{\rm max} = 0.25$. We convert $z_{\rm max}$ to $V_{\rm max}$ values using the Planck 2018 cosmology.

The raw HMF, $\phi(\log[M/M_\odot])$ (see Section 1), is then determined from the sum of the $1/V_{\rm max}$ values within each mass interval (see equation 2) and initially with $w_i = 1$, resulting in the green points shown in Fig. [4](#) (main panel).

Because of the steepness of the HMF, and the significant mass errors, the Eddington bias is expected to be significant. We forward evolve the measured HMF distribution via a set of Monte Carlo simulations, to estimate the size of this bias (w_i). To linear order, $w_i = \phi(M)_1/\phi(M)_{<\rm MC>}$, where $\phi(M)_1$ is our initial measurement, with $w_i = 1$, and $\phi(M)_{<\rm MC>}$ is the average of our Monte Carlo measurements, after perturbing the mass of each group independently. This mass perturbation for each group is given by a lognormal distribution with mean zero and a standard deviation given by the group's $\sigma_{\log_{10} M}$ error. Hence, we are using a forward propagation method to estimate the severity of the Eddington bias. We then use

Table 1. The GAMA HMF values derived in this work adopting a multiplicity lower limit of $N_{FoF} = 5$ and as plotted in Fig. 4. Values above the horizontal bar should be considered credible and those below not. Hence, column 4 rows 1:16 represent our final GAMA HMF. The errors are given as linear fractions.

$\log_{10}(M/M_\odot)$ (Bin centre)	N (Linear)	$\log_{10}\phi$ Mpc^{-3}	$\log_{10}\phi_{corr}$ Mpc^{-3}	$\sigma_{Poisson}$ (Frac.)	$\sigma_{MonteCarlo}$ (Frac.)	σ_{CosVar} (Frac.)	$\sigma_{Combined}$ (Frac.)
15.4	2	−6.943	−6.389	0.71	0.62	0.07	0.94
15.2	4	−6.717	−6.485	0.50	0.32	0.07	0.60
15.0	19	−6.038	−5.599	0.23	0.23	0.07	0.32
14.8	41	−5.702	−5.261	0.16	0.21	0.07	0.26
14.6	67	−5.454	−5.035	0.12	0.21	0.07	0.24
14.4	120	−5.163	−4.735	0.09	0.19	0.07	0.21
14.2	198	−4.791	−4.195	0.07	0.18	0.07	0.19
14.0	256	−4.528	−3.859	0.06	0.23	0.07	0.24
13.8	259	−4.360	−3.659	0.06	0.26	0.07	0.26
13.6	203	−4.250	−3.523	0.07	0.27	0.07	0.28
13.4	196	−4.266	−3.611	0.07	0.32	0.07	0.33
13.2	137	−4.082	−3.277	0.09	0.35	0.07	0.36
13.0	98	−4.181	−3.484	0.10	0.37	0.07	0.38
12.8	48	−4.062	−3.222	0.14	0.43	0.07	0.45
12.6	31	−4.599	−4.213	0.18	0.48	0.07	0.52
12.4	23	−4.171	−3.260	0.21	0.58	0.07	0.61
12.2	16	−4.876	−4.515	0.25	0.67	0.07	0.71
12.0	7	−4.526	−3.616	0.38	0.81	0.07	0.90
11.8	2	−6.148	−6.667	0.71	0.90	0.07	1.00
11.6	2	−5.146	−4.512	0.71	0.92	0.07	1.00
11.4	1	−6.290	−6.628	1.00	0.95	0.07	1.00

this empirically derived Eddington bias per mass bin to debias the observed HMF and recover the intrinsic HMF.

An advantage of this method is that we can use the mass error for each group, rather than an average mass error. The downside is that the Eddington bias correction is only lowest order in the mass errors, and it may be inaccurate for large biases. This is mitigated by the uniform slope of the HMF, as the Eddington bias should be mass invariant for any power-law distribution, except around the 'knee' where the Eddington bias becomes more extreme or incompleteness impedes. The Monte Carlo is repeated 1001 times to minimize statistical noise. We also note here an interesting subtlety: as detection is based on the nth members' flux, yet mass is dependent on the orbital velocity dispersions of the detected members, the Eddington bias does not impact the sample selection but only the masses of the selected systems. Hence, we do not need to apply any mass-based Eddington bias to systems below our detection limit. As detection is based on fluxes that are robust to relatively high precision, we do not believe that an additional detection Eddington bias will be significant.

Finally, we estimate the Poisson, Monte Carlo, and cosmic variance errors for each log mass interval. The former is derived from the square root of the number of groups and the Monte Carlo error from the 16 and 84 per cent quantiles in the $\phi(M)$ values within each mass bin (due to the non-normal behaviour of the HMF distributions). For the cosmic variance errors, we use equation (2) from Driver et al. (2011), to determine a single cosmic variance value based on the total volume surveyed (i.e. ±7 per cent).

Fig. 4 (main panel, red circles) shows the GAMA HMF derived using the method described earlier for a multiplicity limit of $n \geq 5$ (see figures in Appendix A for a range of multiplicity cuts). In the upper panel, we show the direct histogram that peaks at $\sim 10^{13.9}$ M$_\odot$ and information on the selection and final number of groups. In the lower panel, we show the reconstructed HMF using the $1/V_{max}$ weighting (green arrows), and the final Eddington bias-corrected HMF (red data points). The errors include the Poisson and Monte Carlo errors

added in quadrature. The cosmic variance errors are not indicated but are generally less than the Monte Carlo error (see Table 1 Col. 6 versus Col. 7).

The depth of our sample means that our estimate of the HMF applies at an effective redshift that is substantially different from zero: A simple estimate of this redshift can be derived from the mean redshift of our group catalogue, which as stated earlier is $z_{eff} = 0.153$. In practice, however, we will assume that our measurement applies at the slightly smaller round figure of $z_{eff} = 0.1$, and we show theoretical models corresponding to that value. This choice is driven by the desire to compare with other determinations of the HMF from samples that are slightly more local than GAMA (see Section 4). We did consider adjusting the different measurements to allow for slightly different effective redshifts in each case, but the required corrections would be small and within the noise. The evolution of the HMF can be approximated by a shift to smaller masses at higher z and a mass-conserving increase in comoving number density by the same factor. For our fiducial cosmology, the shift between $z = 0$ and 0.1 is 0.08 dex, and the shift between $z = 0.1$ and 0.153 is 0.04 dex.

3.2 Fitting the GAMA HMF with the MRP function

In Fig. 4, the dotted black line shows the recommended MRP function as defined in Murray et al. (2021) but adjusted to our median redshift of $\tilde{z} \approx 0.1$. This adjustment of -0.075 dex in $(M/M_\odot)$ and $+0.075$ dex in $\phi[\log_{10}(M/M_\odot)]$ is based on the predicted evolution of the HMF from $z = 0.1$ to 0.0 (cf. Fig. 1). The definition of the MRP function is repeated here for clarity, and in logarithmic mass intervals, as

$$\phi(\log_{10}(M/M_\odot)) \equiv \frac{dn}{d(\log_{10}(M/M_\odot))}$$
$$= \ln(10)\phi_* \beta \left(\frac{M}{M_*}\right)^{\alpha+1} \exp\left[-\left(\frac{M}{M_*}\right)^\beta\right], \quad (3)$$

Table 2. MRP function fits to various HMF data sets (as indicated) and where, for example, 'GAMA5' refers to the GAMA-only sample with a multiplicity limit of 5. Note that the fits are only valid over the range of the data, i.e. $10^{12.7}$ M$_\odot$ < M_h < $10^{15.5}$ M$_\odot$ except for the final row, 'Omega', where the requirement to converge to the Planck 2018 Ω_M value is included. Note that the fits are for an effective redshift of $\bar{z} \approx 0.1$ and to convert to $z = 0$ one should add 0.075 dex to $\log_{10}(M_*/M_\odot)$ and subtract 0.075 dex from $\log_{10}(\phi*)$.

Sample	$\log_{10}(M_*/M_\odot)$	$\log_{10}(\phi_*)$ Mpc^{-3} dex^{-1}	α	β
GAMA3	$11.65^{+1.37}_{-0.45}$	$-1.87^{+0.03}_{-0.78}$	$-0.78^{+0.24}_{-0.44}$	$0.31^{+0.12}_{-0.02}$
GAMA4	$10.44^{+3.22}_{-1.24}$	$-2.49^{+0.17}_{-0.83}$	$-0.47^{+0.25}_{-1.03}$	$0.24^{+0.22}_{-0.05}$
GAMA5	$13.51^{+0.26}_{-1.51}$	$-3.19^{+0.67}_{-0.28}$	$-1.27^{+0.57}_{-0.18}$	$0.47^{+0.05}_{-0.15}$
GAMA6	$14.42^{+0.28}_{-0.84}$	$-4.32^{+1.03}_{-0.54}$	$-1.75^{+0.35}_{-0.10}$	$0.57^{+0.18}_{-0.17}$
GAMA7	$14.51^{+0.42}_{-0.59}$	$-4.45^{+0.72}_{-0.83}$	$-1.68^{+0.29}_{-0.16}$	$0.60^{+0.40}_{-0.14}$
GAMA8	$14.88^{+0.07}_{-0.81}$	$-5.11^{+1.20}_{-0.21}$	$-1.77^{+0.41}_{-0.04}$	$0.88^{+0.22}_{-0.38}$
OrigErr5	$13.03^{+0.99}_{-0.42}$	$-2.77^{+0.04}_{-1.16}$	$-1.12^{+0.29}_{-0.66}$	$0.45^{+0.19}_{-0.04}$
AngDiam5	$13.52^{+0.47}_{-0.34}$	$-3.22^{+0.30}_{-0.61}$	$-1.60^{+0.21}_{-0.19}$	$0.40^{+0.08}_{-0.04}$
MassA5	$13.14^{+0.71}_{-0.54}$	$-2.98^{+0.26}_{-0.80}$	$-1.45^{+0.32}_{-0.27}$	$0.37^{+0.10}_{-0.04}$
MassAfunc5	$13.68^{+0.21}_{-1.62}$	$-3.46^{+0.84}_{-0.30}$	$-1.35^{+0.74}_{-0.21}$	$0.59^{+0.04}_{-0.24}$
MassWL5	$12.50^{+0.25}_{-0.52}$	$-3.11^{+0.14}_{-0.78}$	$0.07^{+0.72}_{-0.30}$	$0.54^{+0.06}_{-0.07}$
SDSS3	$13.14^{+0.58}_{-0.86}$	$-2.76^{+0.45}_{-0.78}$	$-1.37^{+0.54}_{-0.36}$	$0.51^{+0.15}_{-0.11}$
SDSS4	$13.38^{+0.52}_{-0.09}$	$-3.00^{+0.09}_{-0.78}$	$-1.59^{+0.09}_{-0.29}$	$0.48^{+0.12}_{-0.01}$
SDSS5	$13.38^{+0.62}_{-0.09}$	$-3.00^{+0.07}_{-0.90}$	$-1.57^{+0.12}_{-0.31}$	$0.47^{+0.14}_{-0.00}$
SDSS6	$14.57^{+0.14}_{-0.47}$	$-4.98^{+0.90}_{-0.32}$	$-2.13^{+0.27}_{-0.09}$	$0.80^{+0.07}_{-0.19}$
SDSS7	$14.29^{+0.13}_{-0.78}$	$-4.37^{+1.04}_{-0.26}$	$-1.78^{+0.48}_{-0.10}$	$0.73^{+0.08}_{-0.22}$
SDSS8	$13.82^{+0.70}_{-0.06}$	$-3.70^{+0.02}_{-1.14}$	$-1.45^{+0.13}_{-0.38}$	$0.54^{+0.33}_{--0.01}$
REFLEX II (R)	$14.33^{+0.26}_{-0.38}$	$-4.30^{+0.52}_{-0.53}$	$-1.62^{+0.35}_{-0.27}$	$0.79^{+0.21}_{-0.17}$
GAMA5 + SDSS5 (GS)	$14.35^{+0.36}_{-0.60}$	$-4.38^{+0.93}_{-0.73}$	$-1.96^{+0.37}_{-0.18}$	$0.60^{+0.15}_{-0.10}$
GAMA5 + REFLEX II (GR)	$13.72^{+0.64}_{-0.43}$	$-3.44^{+0.26}_{-0.93}$	$-1.29^{+0.32}_{-0.41}$	$0.55^{+0.26}_{-0.08}$
SDSS5 + REFLEX II (SR)	$14.44^{+0.25}_{-0.38}$	$-4.52^{+0.66}_{-0.58}$	$-1.85^{+0.21}_{-0.18}$	$0.79^{+0.23}_{-0.18}$
GAMA5+SDSS5 + REFLEX II (GSR)	$14.13^{+0.43}_{-0.40}$	$-3.96^{+0.55}_{-0.82}$	$-1.68^{+0.21}_{-0.24}$	$0.63^{+0.25}_{-0.11}$
FIXED-α (FIX)	$14.47^{+0.13}_{-0.15}$	$-4.57^{+0.27}_{-0.26}$	$-1.86^{+0.00}_{-0.00}$	$0.80^{+0.14}_{-0.12}$
Omega	$14.43^{+0.11}_{-0.15}$	$-4.49^{+0.29}_{-0.24}$	$-1.85^{+0.03}_{-0.03}$	$0.77^{+0.11}_{-0.11}$

where ϕ_* is the space density at the characteristic mass point that acts as the vertical normalization, M_* is the characteristic halo mass that acts as the horizontal normalization, α is the low-mass slope parameter, and β is the high-mass exponential softening parameter (see also Trevisan & Mamon 2017). This can also be expressed in linear mass intervals as

$$\phi(M) \equiv \frac{dn}{dM} = \frac{\phi_* \beta}{M_*} \left(\frac{M}{M_*}\right)^\alpha \exp\left[-\left(\frac{M}{M_*}\right)^\beta\right]. \quad (4)$$

Following from this, the total mass density, i.e. the integral of the MRP to zero mass, can be given in terms of the complete Γ function, by

$$\rho_M = M_* \phi_* \Gamma((2+\alpha)/\beta). \quad (5)$$

Note that from equation (5) values of $\alpha > -2$ are required for a finite value for ρ.

We fit the MRP function to our data by minimizing the χ^2 (see equation 6), with the addition of an appropriate factor to account for the empty high-mass bins (in which groups are visible across the full survey volume should they exist), i.e.

$$\sum_{i=1}^{i=n} \left(\frac{\log_{10}(\phi_i) - \log_{10}(\bar{\phi}_i)}{\frac{\sqrt{\Delta\phi_{i,\text{Ran}}^2 + \Delta\phi_{i,\text{MC}}^2}}{(\ln(10)\phi_i)}}\right)^2 + 2\sum_{i=n+1}^{i=n+10} \bar{\phi}_i V_{\text{limit}} \Delta\log_{10} M, \quad (6)$$

where ϕ_i represents our binned measurements (Table 1, Col. 4), $\bar{\phi}_i$ the expectation from equation (3), and σ_i is the data uncertainty of the ith bin (Table 1, Col. 8). For the penalty factor, we calculate $\bar{\phi}_i$ for the first 10 unoccupied bins (as one increases in halo mass from the highest detected group), where V_{limit} is the maximum volume surveyed and $\Delta\log_{10} M$ is the bin width. The penalty factor derives from the exact Poisson probability of finding an empty bin when the expected number of system is non-zero, and it ensures that the fit does not overpredict at the high-mass end where no groups were detected.

The data and errors are shown in Fig. 4 and reported in Table 1. Here, the errors are derived in a posterior fashion from either $\sqrt{(n)}$ statistics (σ_{Poisson}), where n is the number of groups in the bin, or from the Monte Carlo refitting ($\sigma_{\text{MonteCarlo}}$). The errors shown in Fig. 4 are the σ_{Combined} errors (see Table 1, Col. 8) that are the sum in quadrature of σ_{Poisson} and $\sigma_{\text{MonteCarlo}}$ only. The best-fitting MRP values to these data, and for our other selections discussed later, are shown in Table 2. Fig. 5 highlights the covariances of the fitted parameters (as indicated).

From Fig. 4 (main panel), we see that the recovered HMF peaks in the mass bin centred at $M \sim 10^{12.9}$ M$_\odot$, and adopt $M = 10^{12.8}$ M$_\odot$ as our mass completeness limit but see also the discussion below in Section 3.3.5. Note that while $1/V_{\text{max}}$ corrects for the diminishing volume, the method only works up to the point at which all subclasses within the mass range are sampled; i.e. one cannot correct for
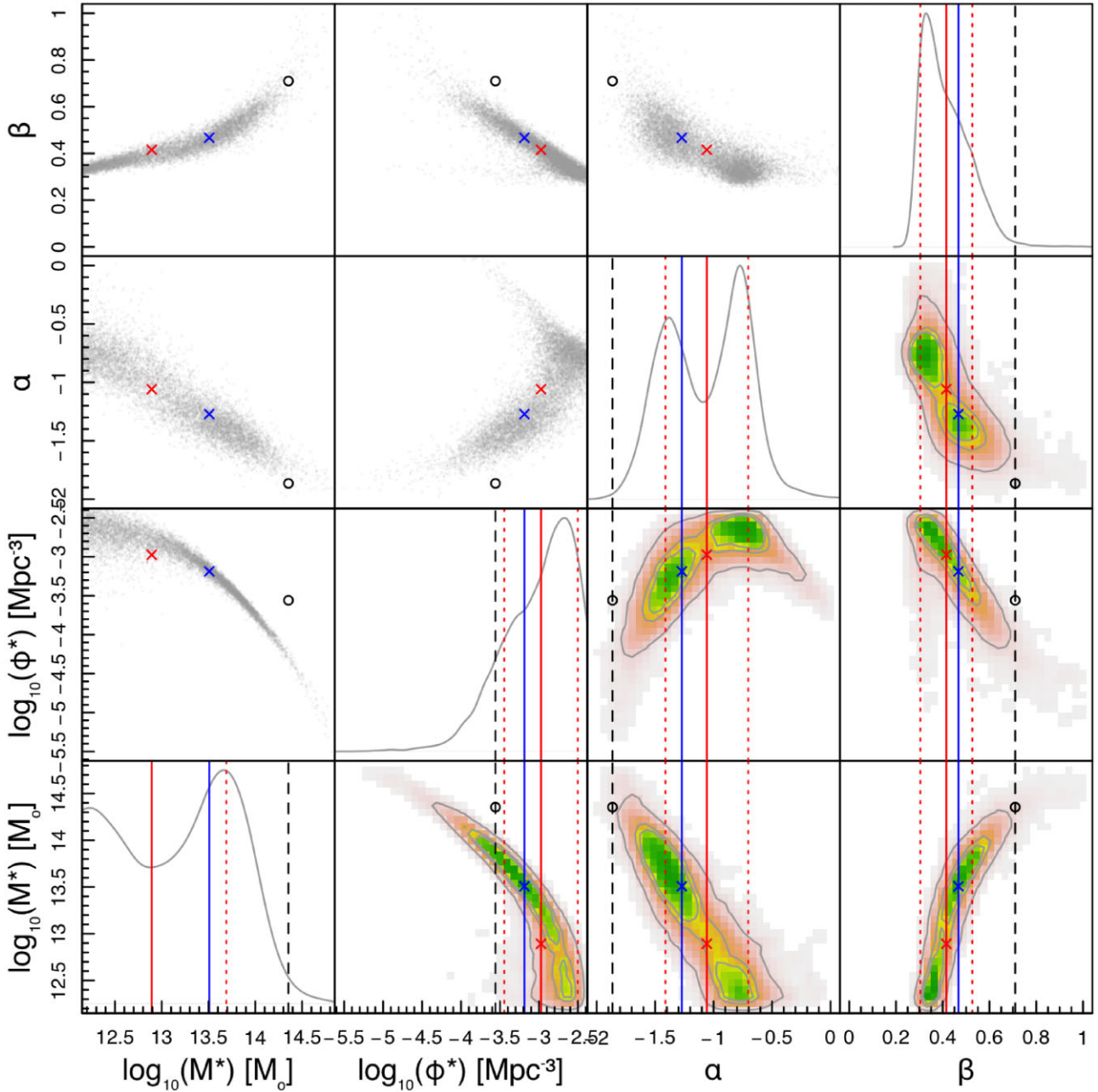
Figure 5. The covariances of the fitted MRP parameters to the data shown in Fig. 4. The blue crosses and blue solid lines show the location of the best fit within each panel. The red cross and lines show the mean of the fitted values, and the red dotted lines the $\pm 1\sigma$ error ranges based on the standard deviation of the distribution. Note that due to the correlation and complex shape of the error distribution the simple mean of the fitted data (red crosses) does not always represent viable fits. Also shown are the parameters recommended by MRP adjusted to $\bar{z} = 0.5$ (black circles). The lower right quadrants show the 1σ, 2σ, and 3σ error contours (grey contours encircling green, yellow and orange shaded regions).

what one does not detect. Eventually, as groups with large flux gaps between their brightest and nth brightest member become undetectable, the mass function gradually becomes incomplete. Here, we will take the empirical approach of only fitting to our mass function up to the point at which this turn down becomes apparent, and this is indicated by the solid (complete bins) and open (incomplete bins) symbols in Fig. 4 (main panel). In due course, this incompleteness needs to be modelled, but once again ties the analysis tightly to simulations, which comes with its own issues (see Section 3.3.5).

Overlaid on the main panel of Fig. 4 is the predicted HMF from Murray et al. (2021) (dashed black line), also using the Planck 2018 cosmology. The data agree within the errors with the HMF prediction, with a similar but slightly shallower low-mass slope and comparable abundance at the characteristic mass. This is in part due to the size of the error bars, which are very much dominated by the Monte Carlo error (see columns 5, 6, and 7 in Table 1). Typically, the average halo mass error in the $N_{\mathrm{FoF}} \geq 5$ sample is $\sigma_{\log_{10} M} \sim 0.25$, i.e. a factor of 2.1, and essentially reflects the significant mass uncertainties acting through the Eddington bias.

The solid blue line shows the optimal MRP functional fit to the GAMA data, while the fainter blue lines show a fraction of the Monte Carlo refits. Note that we Monte Carlo by jostling each individual data point by its allowed random error (σ_{Combined}), and additionally the entire data set systematically by its cosmic variance error (σ_{CosVar}). We then refit again using equation (6). The Monte Carlo MRP fits exhibit a range of curves that encompass the MRP expectation from ΛCDM. The range of the Monte Carlo MRP fitted values is represented in Fig. 5, which shows the covariance of the fitted parameters. Clearly apparent is the tight correlation between M_* and ϕ_*, but we also note the trade-off between M_* and the β parameter. At face value, the range of the individual errors is quite broad, suggesting that the fit is fairly poor; however, this belies the significant covariance of the fitted parameters, which generally form fairly narrow distributions. The black circle shows the ΛCDM expectation from Murray et al. (2021), while the blue crosses our best-fit value. The red cross shows the mean of the individual parameter distributions, which do not necessarily combine to provide a sensible fit. The dotted red lines show the standard deviation of each data set which do not necessarily align with the 1σ, 2σ, and 3σ error contours (grey lines and colour shading).

Hence, we can conclude that while the GAMA HMF data show apparent consistency with expectation, formally the errors do suggest some very mild tension. This is most easily seen in the apparent excess of haloes in the intermediate-mass range in Fig. 4, generally demanding a higher normalization. This tension could potentially be released by modifying (i.e. fitting for) the mass calibration parameter A. However, our preference is to keep this parameter fixed for now, and in due course replace it with an empirically derived value in future analysis. In the meantime, we look to improve our constraint by incorporating literature data sets, in which different fundamental mass calibrations are adopted, and hence averaging over a range of mass assumptions/calibrations. However, before folding in these external data sets, we first discuss some of the systematics at play.

3.3 Some continued digressions

3.3.1 Severity of the Eddington bias

Our measured HMF has a strong dependence on the Eddington bias correction. To emphasize this, we show, as the black line with circles in Fig. 6, the global value for w_i (vertical axis) if we were to adopt the constant mass error indicated on the horizontal axis. Hence, for a *constant* mass error of $\sigma_{\log_{10} M} = 0.5$ we find an amplification, or multiplication of the derived HMF ϕ values of a factor (w_i) of ∼5.5. To some extent, this is acceptable if known and corrected for appropriately, but this approach fundamentally relies on the precision to which the mass errors are known. Ultimately, the smaller the mass uncertainty, the smaller is the required Eddington bias correction, and the more robust the HMF. The histogram in Fig. 6 shows the actual distribution of the mass errors for the full sample (i.e. $N_{\text{FoF}} \geq 3$), with an arbitrary vertical scaling. Ultimately, to keep the Eddington bias manageable (i.e. $w_i < 1.25 \times$) would require mass errors below $\sigma_{\log_{10} M} \sim 0.1$. The difficulty in achieving this may well prove to be a fundamental obstacle in advancing our empirical measurements of the HMF. However, we once again note that it is not necessarily the size of the Eddington bias that matters most but our ability to correct for it robustly.
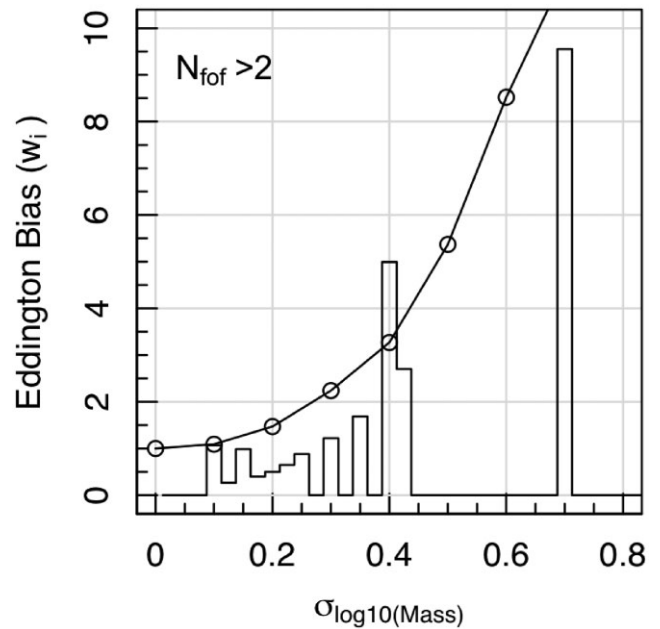

Figure 6. A demonstration of the severe impact of the mass uncertainty ($\sigma_{\log_{10} M}$) on the order of magnitude of the mean Eddington bias correction (circles and connecting lines). Also shown, against arbitrary units, is the histogram of the mass error distribution for the GAMA groups used to derive our HMF.

3.3.2 The impact of a larger mass error

As noted in Fig. 3, our adopted errors, while consistent with weak lensing (Viola et al. 2015) and the studies of Old et al. (2014), are a good deal smaller than those originally advocated by Robotham et al. (2011). Here, we rerun our HMF calculation again with a multiplicity limit of 5, but this time using the original errors. We show the perturbations of the recovered HMF relative to the original as a fraction in Fig. 7 (lower panel, dark blue line). In general, the agreement is good (i.e. within the error bars), except at high masses where the larger error gives rise to a systematic bias that exceeds the Monte Carlo errors. We believe, for the reasons outlined earlier, that the original mass errors were overestimated. Note that Fig. A2 (centre right) shows the derived HMF using the original mass errors.

3.3.3 The impact of alternative mass estimates

Fig. 7 (lower panel) also shows the perturbations from a recalculation of our HMF for $N_{\text{FoF}} = 5$ but now using MASSA with $A = 10$ (cyan line), MASSAFUNC (orange line), and the masses derived via weak lensing from equation (38) of Viola et al. (2015) (green). As can be seen, the data move fairly minimally for MASSA (essentially the scaling one would expected from moving from $A = 10.0$ to 13.9), and MASSAFUNC (barely noticeable), but significantly with comparison to the weak lensing masses and in particular the high-mass end is dramatically impacted, with the green curve falling off the plot at $10^{14.5} \, M_\odot$. It is hence possible that weak lensing may be less sensitive to higher mass systems, possibly because of their relatively low space density. In this case, the impact of trying to use the weak lensing mass predictions becomes catastrophic at the high-mass end.
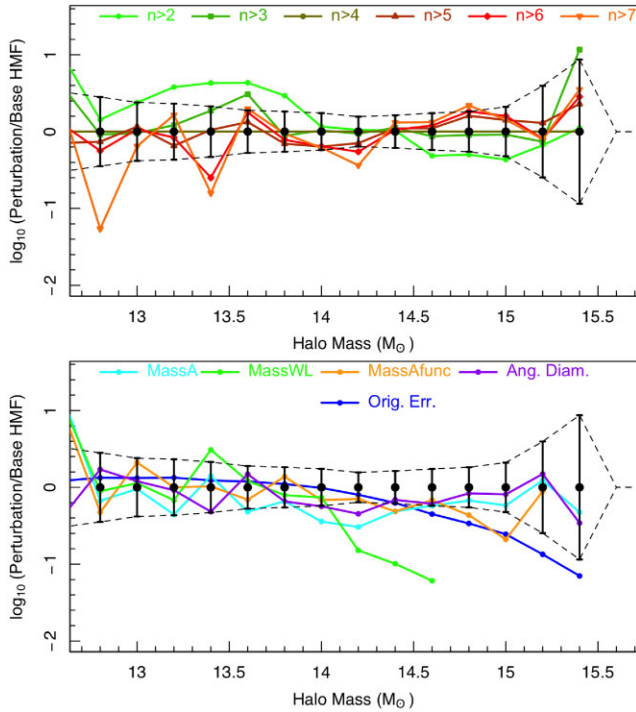
Figure 7. (Both panels) The variation of the GAMA HMF based on different underlying choices as indicated in the labels. The black data points show the base GAMA HMF with associated errors and which is taken as the $N_{FoF} \geq 5$ case. The upper panel shows variation based on multiplicity cut while the lower panel different choices in the analysis process. Generally, in both panels the variation is enclosed within the errors with the exception of the weak lensing masses (lower panel, green).

3.3.4 Multiplicity cuts

In Fig. 7 (upper panel), we show the perturbations to our mass function if we adopt a range of multiplicity cuts from >2 to 7 (as indicated). In each case, the sample size is significantly reduced but so too are the mass errors. Above our completeness limits, we see this impact as a systematic bias towards higher abundances at higher masses but generally the data lie within the quoted errors, which is reassuring. We also note that for very low multiplicity cuts we start to see an excess at lower halo masses that might suggest either contamination or incompleteness starting to impact high-multiplicity cuts (or both).

3.3.5 The onset of incompleteness

At some point, the HMF turns down, despite the $1/V_{max}$ correction. This will typically occur when subsets within a bin are no longer represented at all, for example, groups where the fifth brightest member is fainter than our detection threshold at our lower redshift limit. An obvious solution is to determine incompleteness via comparison to simulations. The key issue here is that the precise flux distribution of intrinsically faint galaxies within a halo is poorly constrained within simulations. Essentially, this pathway requires the simulations to be fundamentally correct at a level at or below the mass resolution of the underlying numerical simulation. This is perhaps best illustrated by considering a Milky Way halo, where the stellar mass of the fifth most massive member is about $1000\times$ below that of the Milky Way, or $\sim 10^9$ M$_\odot$. At this level, the exact prescription adopted for dynamical friction, which dictates merger time-scales,
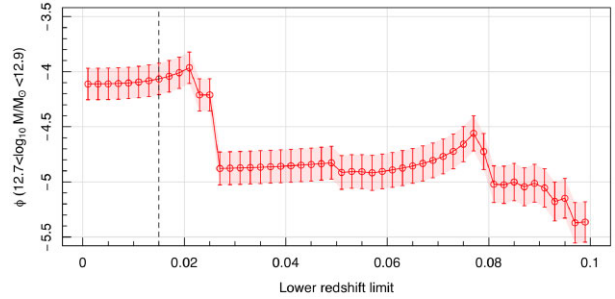
Figure 8. The dependence of the density of haloes in the range $10^{12.7}$–$10^{12.9}$ M$_\odot$ on the lower limiting redshift used for the derivation of the GAMA HMF.

etc., becomes important. Hence, by calibrating to a specific mock, one ties one's detection limit, or incompleteness correction, to a specific semi-analytical prescription that may or may not match reality.

The alternative is to find an empirical pathway. Here, we propose that incompleteness becomes more apparent as one imposes arbitrarily more stringent selection limits, e.g. by increasing our lower redshift limit cut or by increasing our multiplicity constraint. Fig. 7 (upper panel) shows how each of the density bins varies with multiplicity cut. Here, we see that in the lowest bin used in our fitting, i.e. $10^{12.7} < \log_{10} M/M_\odot < 10^{12.9}$ is relatively stable, within the quoted error, suggesting resilience to incompleteness. Similarly Fig. 8 shows how the density in the same halo mass bin varies as we increase the minimum redshift from 0.0 to 0.1. Once again, one can see that as we increase the minimum redshift limit, the density remains stable until a limit of 0.02 at which point the density drops dramatically, and we interpret as the onset of irrecoverable incompleteness.

While the empirical method has the advantage of not requiring any knowledge of the intrinsic properties of the groups a priori, its weakness is that it cannot correct for entirely dark haloes in which no gas has been processed into stars. In this sense, our HMF is therefore a measure of the 'astrophysically active' haloes only (i.e. haloes that are purely plasma filled and where no star formation or gas cooling has occurred). As the fraction of 'astrophysically inactive' haloes is predicted to increase with decreasing halo mass, one might expect that at some point our empirically measured HMF will underpredict the HMF advocated by simulations.

3.3.6 The impact of switching to the angular diameter distance

Fig. 7 (lower panel, purple line) shows the perturbations when defining group size using the angular diameter distance rather than the comoving distance (as discussed in Section 2.1.2). At the redshifts we are considering, this effect is fairly minimal and remains within the errors.

For all of the variant HMFs, we report the fitted MRP HMF values in Table 2 and show the figures in Appendix A. Overall, these results are reassuring in that the errors from our favoured GAMA HMF fit generally encompass the range of variation we see through the different choices. The principal exception is at very high masses where the use of the original errors or weak lensing mass constraints would lead to a dramatically different and more sharply truncated HMF. We take GAMA5 (i.e. the GAMA sample with $N_{FoF} \geq 5$) as being our optimal parameter set, and note the tendency for slightly higher multiplicity cuts to favour higher $M*$ and lower $\phi*$ but also note the strong degeneracy of these two parameters.

Table 3. The values derived in this work for the SDSS group catalogue of Tempel et al. (2017) and plotted in Fig. 11 (as purple data points). As for Table 1, column 4 rows 1:16 represent our derived SDSS HMF. The errors are given as linear fractions.

$\log_{10} (M/M_\odot)$ (Bin centre)	N (Linear)	$\log_{10} \phi$ $\mathrm{Mpc}^{-3}\,\mathrm{dex}^{-1}$	$\log_{10} \phi_{\mathrm{corr}}$ $\mathrm{Mpc}^{-3}\,\mathrm{dex}^{-1}$	$\sigma_{\mathrm{Poisson}}$ (Frac.)	$\sigma_{\mathrm{MonteCarlo}}$ (Frac.)	σ_{CosVar} (Frac.)	$\sigma_{\mathrm{Combined}}$ (Frac.)
15.05	4	−6.889	−5.989	0.50	0.41	0.07	0.64
14.95	5	−6.792	−6.094	0.45	0.37	0.07	0.58
14.85	11	−6.450	−5.676	0.30	0.28	0.07	0.41
14.75	14	−6.345	−5.672	0.27	0.24	0.07	0.36
14.65	26	−6.055	−5.282	0.20	0.24	0.07	0.31
14.55	25	−6.093	−5.535	0.20	0.20	0.07	0.29
14.45	60	−5.708	−4.952	0.13	0.18	0.07	0.22
14.35	71	−5.638	−4.970	0.12	0.18	0.07	0.21
14.25	102	−5.460	−4.768	0.10	0.17	0.07	0.20
14.15	152	−5.246	−4.471	0.08	0.16	0.07	0.18
14.05	183	−5.057	−4.210	0.07	0.16	0.07	0.18
13.95	240	−4.985	−4.173	0.06	0.16	0.07	0.17
13.85	302	−4.755	−3.798	0.06	0.15	0.07	0.16
13.75	332	−4.650	−3.663	0.05	0.16	0.07	0.17
13.65	362	−4.586	−3.597	0.05	0.16	0.07	0.17
13.55	367	−4.529	−3.532	0.05	0.16	0.07	0.17
13.45	391	−4.456	−3.428	0.05	0.16	0.07	0.16
13.35	351	−4.393	−3.327	0.05	0.17	0.07	0.18
13.25	338	−4.359	−3.270	0.05	0.17	0.07	0.18
13.15	302	−4.272	−3.103	0.06	0.19	0.07	0.20
13.05	258	−4.422	−3.398	0.06	0.20	0.07	0.21
12.95	217	−4.254	−3.041	0.07	0.21	0.07	0.22
12.85	182	−4.472	−3.447	0.07	0.22	0.07	0.23
12.75	152	−4.633	−3.713	0.08	0.23	0.07	0.24
12.65	111	−4.562	−3.518	0.09	0.25	0.07	0.27

4 INCLUDING EXTERNAL HALO MASS FUNCTION CONSTRAINTS

Despite the importance of the HMF, there have been relatively few attempts at direct empirical measurement, although we note the efforts in measuring the velocity dispersion distributions. This is primarily due to the difficulty and complexity in constructing group catalogues that typically require large-scale spectroscopic programmes or wide-area X-ray observations. Most notable are the HMFs derived by the 2dFGRS team (2PIGG; Eke et al. 2006), and that derived from X-ray measurements with *ROSAT* (e.g. REFLEX II; Böhringer et al. 2017). In addition, attempts have been made to study the stellar–mass halo relation using the SDSS group catalogue. Here, we attempt to briefly review and combine these external data sets to improve our estimate of the MRP parameters.

4.1 2PIGG

The 2dFGRS team (Colless et al. 2001) measured the distances to ∼250 000 galaxies at greater than 80 per cent spectroscopic completeness. From these data, a group catalogue was constructed by Eke et al. (2004) using a Percolation Inferred algorithm. This is in essence very similar to the friends-of-friends algorithm employed by the GAMA team (Robotham et al. 2011), with linking lengths calibrated to numerical simulations.

The 2PIGG catalogue resulted in ∼29 000 pairs or groups, and over 7000 with 4 or more members, a median redshift of ∼0.11, and a median velocity dispersion (σ) of ∼260 km s^{-1}. In Eke et al. (2006), the team published the 2dFGRS HMF and found good agreement with the ΛCDM expectation, given the associated errors, over the mass range of $10^{13.5}$–$10^{15.25}$ M$_\odot$.

The 2PIGG HMF data were derived for a cosmology with $\Omega_M = 0.3$ and $\Omega_\Lambda = 0.7$ and with $H_0 = 100$ km s^{-1}. Here, we use the reported 2PIGG HMF values (Eke et al. 2006), and modify the group masses and number densities by h^{-1} and h^3, respectively, but do not attempt to correct for the small shift from the 2PIGG native cosmology to the Planck 2018 cosmology. We note in our final analysis we will not use 2PIGG results, but do include them in our figures for completeness. In Figs 11 and 13, the 2PIGG data are shown as grey data points and look to be consistent with the other data sets albeit with a slightly flatter slope.

4.2 SDSS

Recently, Tempel et al. (2017) applied their friends-of-friends group-finding algorithm to the SDSS DR12 (Alam et al. 2015). The final catalogue contains a total of 88 662 galaxy pairs or groups, 37 365 with 3 or more members and 10 087 with 5 or more members. This is derived from the SDSS DR12 parent catalogue of 584 449 galaxies within a 7221 square deg area of the SDSS Main Survey footprint (see also Tempel et al. 2014).

A particular focus of the work was the identification of merging groups, which can often be mistaken for a single high-mass cluster, and care was taken to disentangle these cases. The online catalogues were downloaded from http://cosmodb.to.ee. The catalogue contains M_{200} values that are derived from a combination of the velocity dispersions, which are also based on the GAPPER method to convert the redshift distributions to velocity dispersions, and the group sizes given as R_{vir}. Old et al. (2014) conducted a fairly exhaustive study of mass estimates and derived errors on the masses for three mass intervals (see their table 3). Old et al. (2014) report approximate mass errors appropriate for the Tempel et al. (2014) group finder, i.e.
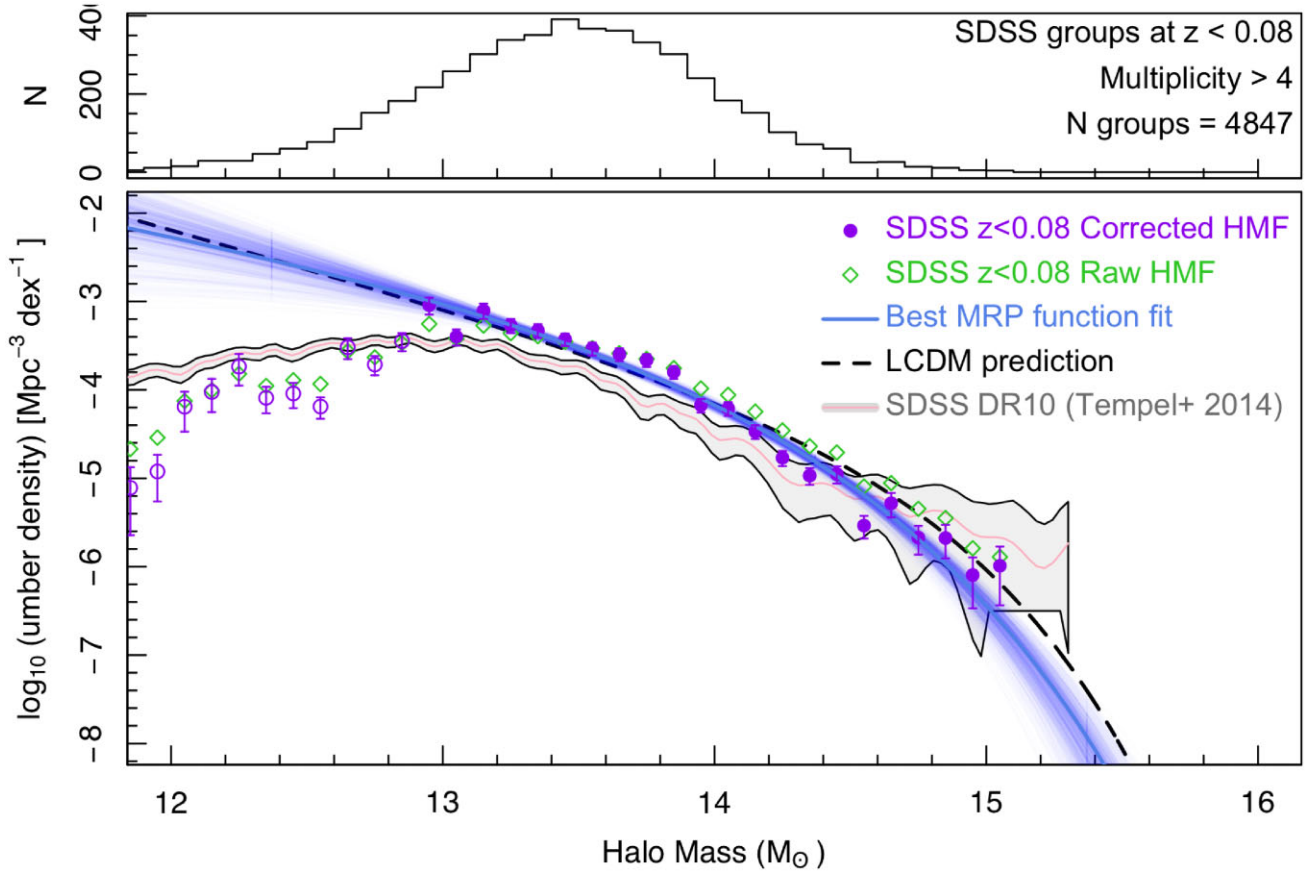
Figure 9. As for Fig. 4 except now for the SDSS data of Tempel et al. (2017).

$\sigma_{\log_{10} M} \approx 0.25$ at 10^{15} M$_\odot$ rising to $\sigma_{\log_{10} M} \approx 0.35$ at $10^{13.0}$ M$_\odot$ (our cut-off for the SDSS data). However, these do not include the impact of multiplicity that we see as the dominant error. It is worth noting that Tempel et al. (2014) attempt to circumvent the mass calibration issue by fixing A to the value implied from a pure NFW mass profile.

We now implement an identical method as described for GAMA to determine the SDSS HMF. The results of our derived SDSS HMF are tabulated in Table 3 to the nominal mass limit of $10^{12.9}$ M$_\odot$, and plotted in Fig. 9 as the purple data points. Also shown in Fig. 9 are the volume-limited (-18) results from Tempel et al. (2014). Contrary to GAMA, the SDSS data at higher masses tend to fall marginally below the ΛCDM expectation, and in general have a slightly lower amplitude. We note that the data are also slightly inconsistent with the SDSS DR10 estimate of Tempel et al. (2014). This could be due to the distinct methods applied, $1/V_{max}$ with Eddington bias correction versus a purely volume-limited sample (i.e. constant V_{max} without an Eddington bias correction). It could also be due to the effort invested in the DR12 catalogue (Tempel et al. 2017), in identifying and separating erroneously merged groups, leading to a modest reduction of high-mass systems and a modest increase in intermediate-mass systems.

Fig. 10 shows the covariance of the fitted parameters that are generally better behaved than for GAMA (cf. Fig. 5). Again, we see a slight offset in the M_* parameter but note the degeneracy between β and M_*. We also see a slightly steeper low-mass slope of between $\alpha = -1.57^{+0.12}_{-0.31}$ and closer to expectation ($\alpha = -1.89$).

4.3 *ROSAT* and REFLEX II

Probably the most compelling HMF measurements to date come from X-ray wavelengths, and in particular the *ROSAT* All Sky Survey data set. From this data set, the *ROSAT*-ESO Flux Limited X-ray Galaxy Cluster Survey (REFLEX II) was formed containing 910 clusters out to $z = 0.4$ (Böhringer et al. 2013). These data were combined into an X-ray luminosity function in Böhringer, Chon & Collins (2014) and used to derive constraints on Ω_M and σ_8 for a specified halo model. In Böhringer et al. (2017), a sample of 863 clusters from the same sample were transformed into a mass function using the luminosity–mass relation (L_X–M) (see Böhringer et al. 2017). These data are shown in Fig. 11 as the green diamonds, and contain 20 clusters per bin except for the highest mass bin, which contains 3 clusters. The errors shown are simply $\sqrt{n}$. Uncertainty in the masses is estimated to be $\sigma_{\log_{10} M} \sim 0.1$ and hence an expected Eddington bias of $\sim \times 1.25$ (see Fig. 6). We do not correct for this. We also make no allowance for the fact that the effective redshift for this sample will be slightly lower than for GAMA.

4.4 Joint constraints

Fig. 11 shows the combined data set (as indicated). These form a data set that scatters consistently around the expectation curve from ΛCDM (dashed black line). This agreement now extends over a mass range from $10^{15.5}$ to $10^{12.7}$ M$_\odot$, significantly expanding on previous studies and providing strong corroboration of the ΛCDM prediction.
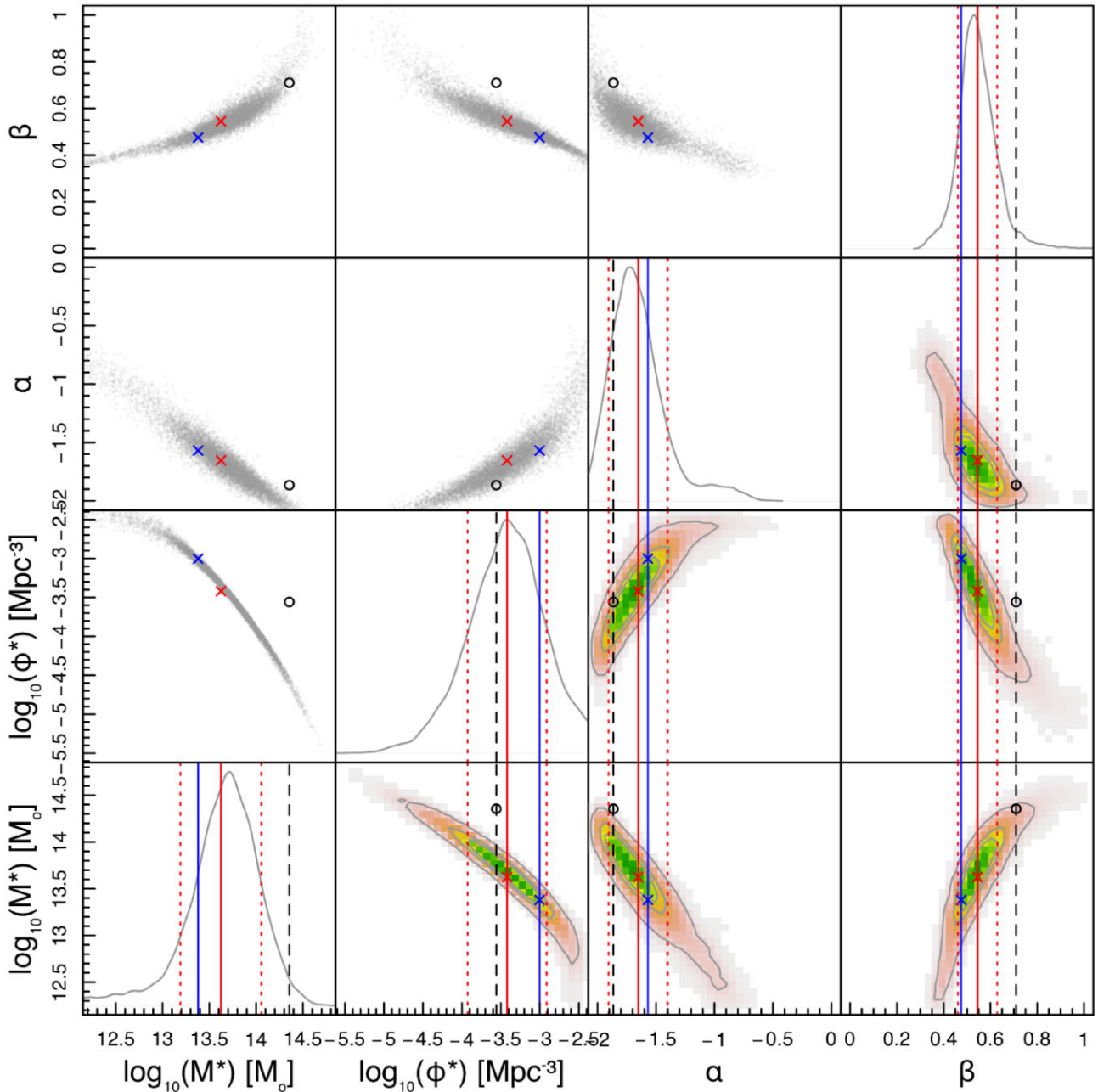
Figure 10. As for Fig. 5 except now for the SDSS data of Tempel et al. (2017).

In general, the X-ray data (green data points) dominate the 'knee' region, providing the tightest error constraints, while the GAMA and SDSS data (red and purple data points, respectively) provide leverage on the low-mass slope. The lack of detections in all three surveys at high mass, within their respective volumes, helps in constraining the high mass turn-down.

We fit the combined GAMA, SDSS, and REFLEX II (GSR) data (and all combinations thereof), with the MRP function as before (see equation 3). We find a good fit given by the blue dashed line with perhaps some greater scatter in normalization. This reflects both the cosmic variance now acting independently on the three data sets and the independent methodologies for absolute mass calibration (i.e. the uncertainty in A). The fit has a convergent low halo mass slope of $-1.68^{+0.21}_{-0.24}$, just consistent with expectation ($\alpha = -1.89$; Murray

et al. 2021). Integrating this curve to zero mass yields a total mass density of about half the expected value (see Fig. 11 inset panel), although the range of values from our Monte Carlo simulation (inset panel red shading) does enclose the Planck 2018 value (vertical black dashed line). The uncertainties on the MRP parameters were again derived by independently perturbing each of the GAMA, SDSS and REFLEX II data points by their errors, and each data set by their cosmic variance error, and refitting to form the spread of blue lines, showing the plausible range of fits. The uncertainty and covariances of our final fitted parameters are represented in Fig. 12; in general, these are well behaved with most values of α convergent (i.e. $\alpha > -2$).

Fig. 13 shows (upper) our best-fitting MRP function over a broader halo mass range; (centre) the same distribution but now expressed
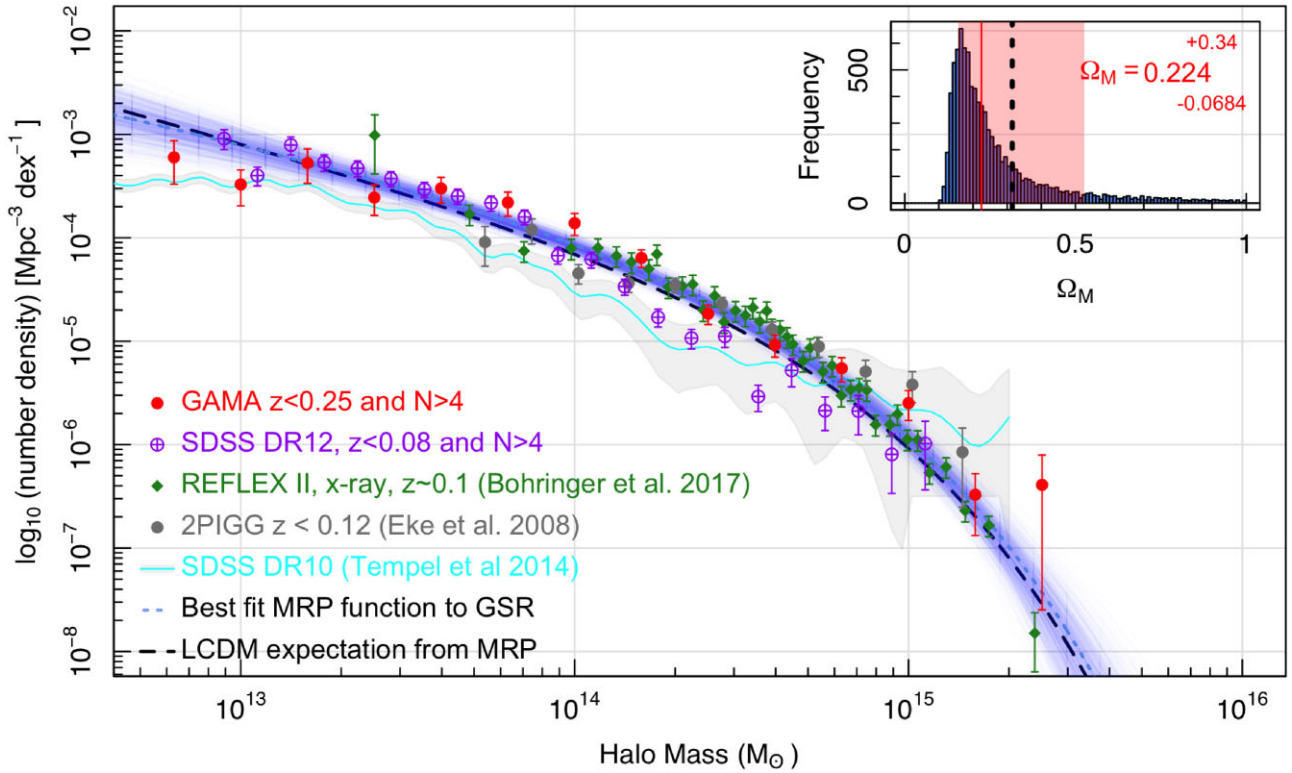
Figure 11. The combined empirical HMF data (as indicated). Shown as black and blue dashed lines are the ΛCDM prediction and the best MRP function fit to the combined GAMA, SDSS, and REFLEX II data along with the spread of MRP fits in blue that show the results from our Monte Carlo refitting. The inset panel shows the integral of the Monte Carlo MRP fits to zero mass (blue histogram) with the red band showing the 1σ error range. The vertical black dashed line shows the Planck 2018 value for Ω_M.

in terms of the contribution to the mass density (rather than number density); and (lower) the cumulative contribution, by integrating from high mass to low mass, and expressed as a fraction of the Planck 2018 matter density ($\Omega_M = 0.3147 \pm 0.0074$). The MRP fit to the GAMA data only (GAMA5) is shown in red, and the fit to the final combined GAMA + SDSS + REFLEX II data is shown in orange. The joint fit has significantly tighter errors not represented here, but more apparent in Figs. 14, which show all the MRP fitted parameters for all data combinations explored in the main text and appendix.

We now consider two extensions: first, fixing α, and secondly, incorporating the Planck 2018 Ω_M prior. We show in Fig. 13 in green the optimal MRP fit if we fix the α parameter to the value recommended by Murray et al. (2021). The red, orange, and green all match the data reasonably well, but as can be seen in the lower panel, all three either underpredict or overpredict the total matter density when integrated to very low halo masses. Hence, we now fold in the Planck 2018 Ω_M value as an additional constraint on the MRP fitting process. To do this, we minimize the following expression:

$$\frac{1}{N_{bins}} \sum \frac{[\phi(M_{emp}) - \phi(M_{mod})]^2}{\sigma_{Combined}^2}$$
$$+ \frac{\left[\int_0^\infty (M_h . \phi_{(M_*, \phi_*, \alpha, \beta)} dM_h / \rho_{crit}) - \Omega_M\right]^2}{\sigma_{\Omega_M}^2}. \quad (7)$$

Implementing this strategy results in the cyan curve in Fig. 13, which now very closely matches the expectation curve (black line) and by construction integrates to the Planck 2018 matter density value.

Note that to some extent this is not entirely surprising, as the data now primarily constrain the shape of the high-mass end (i.e. M_*, ϕ_*,

and β), while the Ω_M constraint is then forcing the low-mass slope parameter. That most data within their errors overlap with this fit is reassuring, but does perhaps indicate some mild mass bias in the G^3C mass estimates at the lower halo masses. This is perhaps also indicated in the weak lensing mass estimates, and it is noticeable that the HMF based on the weak lensing masses, while fitting poorly at the high-mass end, fits better in the 10^{13}–10^{14} $M_\odot$ range (see Fig. A2, centre left).

Hence, it is plausible that at high halo masses, velocity dispersion mass estimates are more robust, while at lower halo masses (where interlopers may be more prevalent), weak lensing masses are more robust. This does open a pathway to constructing HMFs from the combination of both methods, which we leave for future study. Nevertheless, it has become clear through this work that refining our mass estimates and uncertainties is critical, even more so than larger or lower halo mass samples.

The parameters of all the fits shown in Fig. 13 and in the various plots throughout this paper are listed in Table 2. Our strong recommendation is to adopt the values using the Ω_M constraint when extrapolating to halo masses below $10^{12.7}$ $M_\odot$, and to use the combined (i.e. GSR data) MRP fit when seeking to represent the data, which should be deemed valid over the range of $10^{12.7}$–$10^{15.8}$ $M_\odot$.

New survey programmes such as DESI and WAVES will soon produce much larger group catalogues, but it is clear that the following two factors will be critical if we are to advance our empirical measurement of the HMF:

(1) High spectroscopic completeness (>90 per cent) is critical in ensuring that low-mass haloes are detected and sparse haloes, or those with mass gaps, are not biased against.
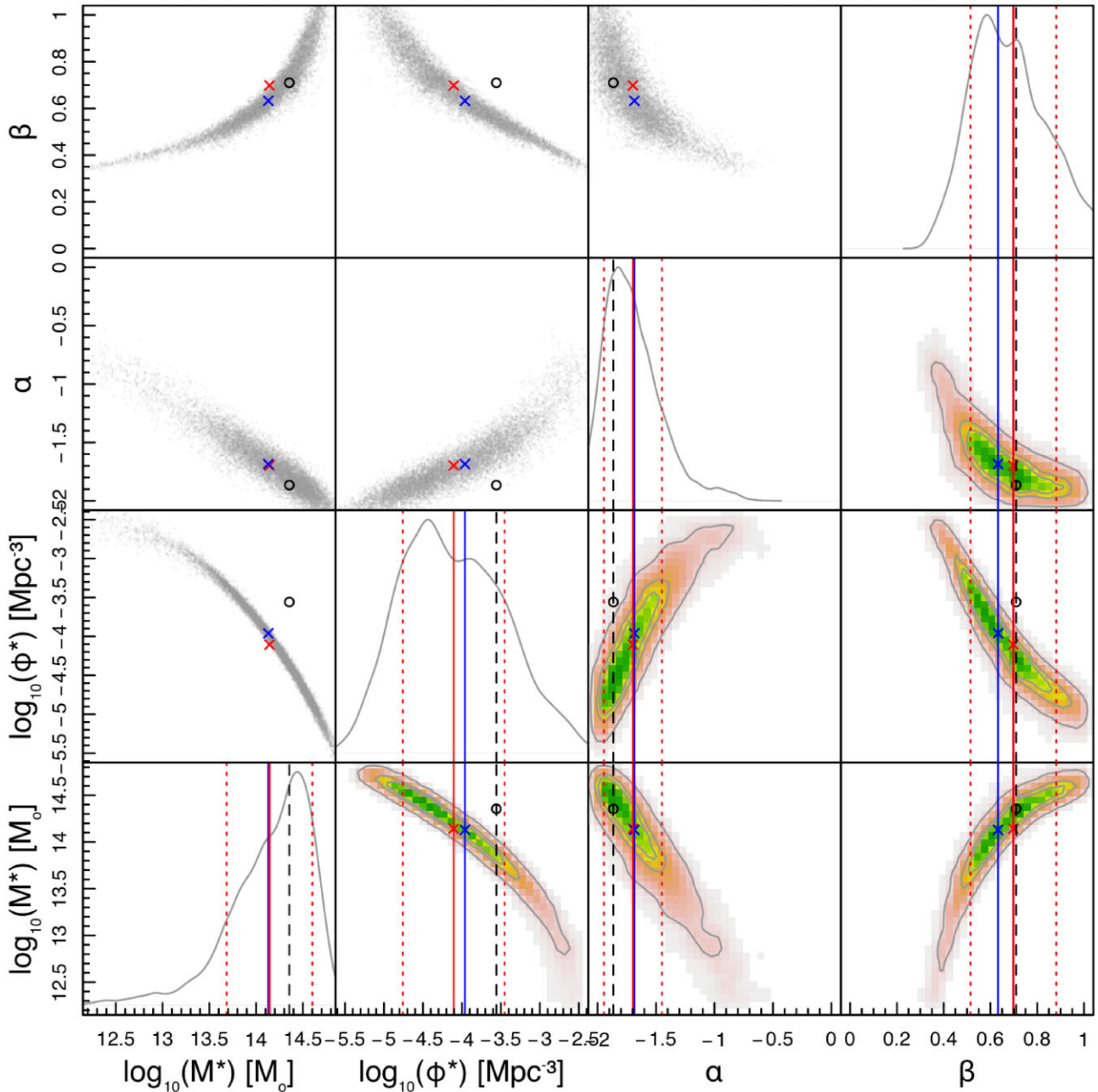
Figure 12. The covariances of the final fitted parameters to the combined GAMA, SDSS, and REFLEX II data.

(2) Significant work needs to be done to improve our mass estimates of galaxy groups especially at low multiplicity and low masses, and this should include comparison of velocity dispersion, weak lensing, and other mass estimates on a halo-by-halo basis as well as for halo populations.

Overall from our work, and from studies based on simulations by Chauhan et al. (2021), we see that it is important to sample at least five members of a galaxy group in order to construct a credible mass estimate and hence a robust HMF. It is sobering to note that for the Local Group this implies probing down to NGC 3109, or the small magellanic cloud, which are about 1000× fainter than the Milky Way or Andromeda.

5 SUMMARY

In this work, we have attempted to reconstruct the HMF via a predominantly model-free empirical pathway, and to highlight the key areas for future consideration along the way. In general, we conclude that over a broad range in halo mass we can confirm the form and amplitude of the HMF, as predicted from numerical simulations and analytical calculations. In particular, we find the dominant error to be the Eddington bias, which arises from the significant mass uncertainties inherent in group determination. To second order, significantly larger samples are also required and over broader local volumes to probe to lower halo masses with meaningful statistics. In combination with X-ray data, we see good consistency, and hence complementarity, between the GSR data. In combination, these data sets are almost enough to constrain the functional form
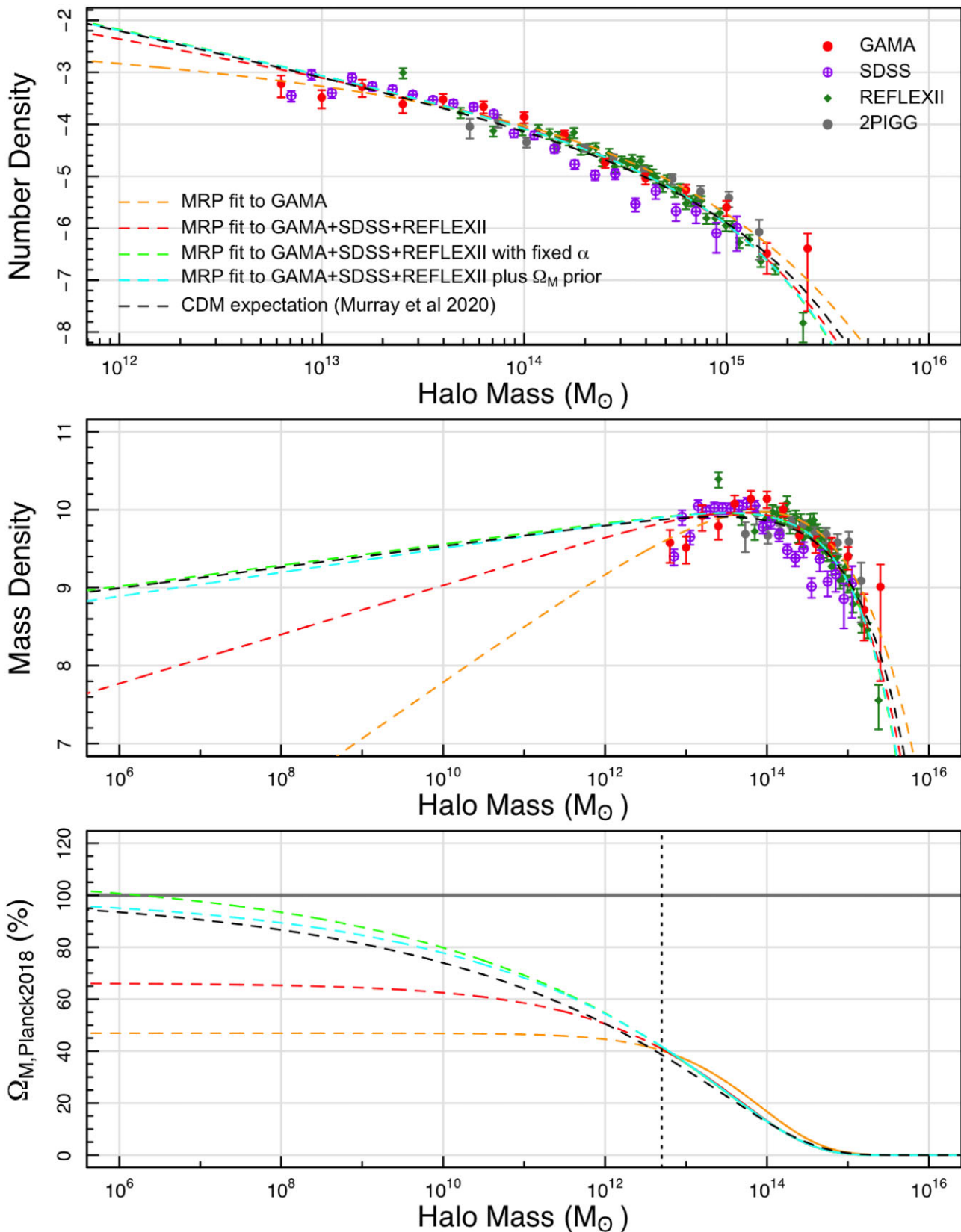
Figure 13. Various fits to the data (as indicated) and showing (top panel) the HMF from Fig. 11 but now over a broader range, (central panel) the contribution of each mass interval to the total density, and (lower panel) the cumulative contribution of the various models to the Planck 2018 mass density. The vertical dashed line in the lower panel indicates the halo mass limit to which our data extend.
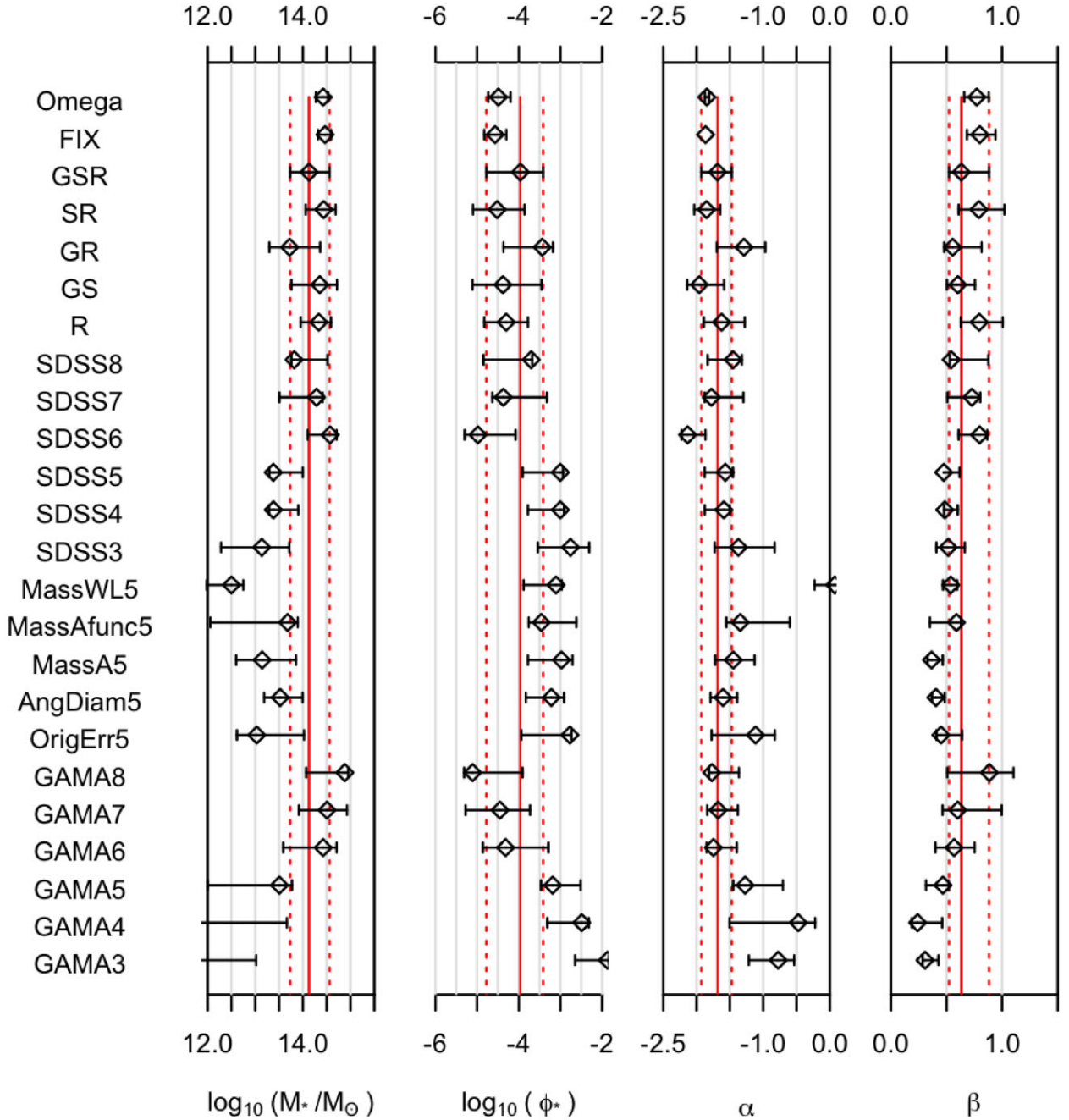
Figure 14. The full set of our fitted MRP results highlighting the variation through our various trials and digressions. The GSR data set is our final favoured fit and the red solid and dashed lines show the mean and errors of our best-fitting parameters extrapolated across the plot for comparison purposes. In general, most fits are consistent with our final fitted parameters. Note also that the errors plotted in this fashion do not incorporate the strong covariances between the four MRP parameters.

of the HMF, and we find an MRP function fit with the following parameters:

$$\log_{10}(\phi_* \, \mathrm{Mpc}^3) = -3.96^{+0.55}_{-0.82},$$
$$\log_{10}(M_* \, \mathrm{M}_\odot^{-1}) = 14.13^{+0.43}_{-0.40},$$
$$\alpha = -1.68^{+0.21}_{-0.24},$$
$$\beta = 0.63^{+0.25}_{-0.11}.$$

Note that the MRP fit is for an effective redshift ($\bar{z}$) of $\approx$0.1 and to convert to $z = 0$ one should add 0.075 dex to $\log_{10}(M_*/\mathrm{M}_\odot)$ and subtract 0.075 dex from $\log_{10}(\phi*)$.

Fig. 14 shows graphically the complete set of all the MRP fits shown in Table 2, and it generally portrays a consistent picture (i.e. most error bars encompass the favoured values). Our final MRP parameters that best represent the data are the third from top value (GSR), and the red lines trace the final fitted values down the figure. It is clear that the REFLEX II data are the dominant data set and currently the X-ray pathway looks like the more secure method to derive the HMF. Nevertheless, the inclusion of the GAMA and SDSS data does significantly tighten the error bars of the fit while remaining consistent with the REFLEX II-only values.

At this stage, it is worth noting that almost *all* the fits are formally convergent, but the error ranges include divergent solutions. In general, the implied Ω_M values are consistent with expectation but with relatively broad errors. For example, our combined GSR fit returns the range of Ω_M values shown in Fig. 11 (inset panel) with the median and 16/84 per cent quantiles as indicated by the vertical red solid line and red band, respectively. Shown in black is the Ω_M expectation from Planck 2018. If we use the Planck 2018 Ω_M value as a prior, then we can recover significantly more stringent MRP fitted values, with quite modest errors, which by design converge to the expected dark matter density. These values are

$$\log_{10}(\phi_* \, \mathrm{Mpc}^3) = -4.49^{+0.29}_{-0.24},$$
$$\log_{10}(M_* \, \mathrm{M}_\odot^{-1}) = 14.43^{+0.11}_{-0.15},$$
$$\alpha = -1.85^{+0.03}_{-0.03},$$
$$\beta = 0.77^{+0.11}_{-0.11}.$$

Note that the MRP fit is for an effective redshift ($\bar{z}$) of ≈ 0.1 and to convert to $z = 0$ one should add 0.075 dex to $\log_{10}(M_*/\mathrm{M}_\odot)$ and subtract 0.075 dex from $\log_{10}(\phi*)$.

We note that there is no real rationale for expecting the HMF to observe a strictly power-law distribution to zero mass, but the test does demonstrate plausible consistency between the preferred MRP values, the Planck 2018 matter density value, and our combined GSR data.

While a stringent independent constraint on Ω_M from an HMF analysis alone is not yet viable, we can ask how much of the total matter density predicted by Planck 2018 is resolved into haloes down to our mass limit. Integrating down to $M_h = 10^{12.7} \, \mathrm{M}_\odot$, we find approximately 41 ± 5 per cent of the expected matter content (regardless of which fit is adopted). This is significant, as it supports the notion that the majority of mass is contained within group haloes, and suggests that it should be possible to build direct dark matter maps from galaxy group catalogues. Such maps would have significantly higher resolution than that achievable via weak lensing, redshift space distortions, or peculiar velocity studies.

Finally, it is worth reiterating that our mostly empirically derived HMF shows broad general agreement with the expectation from ΛCDM, and in doing so provides some confirmation of ΛCDM. However, it is also worth highlighting that this also represents a coming of age of galaxy group catalogues. This is important, as most simulations and observations highlight how the galaxy formation process is strongly dependent on the underlying dark matter halo mass. This is perhaps most obvious not only in the numerical studies of star formation efficiency as a function of halo mass (Behroozi, Wechsler & Conroy 2013; Wechsler & Tinker 2018), but also in the transition from high-mass haloes dominated by hot plasma to low-mass haloes dominated by cold gas and the 'goldilocks zone' in which star formation is most efficient.

Paramount to capitalizing on a group-centric approach to extragalactic astronomy is the need for robust masses. In this work, as with most studies, we rely on the viral theorem embodied in the very simple equation (1) and the calibration of a simple constant A via simulations. This approach does raise concerns over non-orthogonality between the measurements and the models (circularity?), but also the simple virial mass estimate clearly does not use all the information at hand, and does not acknowledge or incorporate factors such as partial virialization, ongoing/lingering halo mergers, halo morphologies, and the additional information encoded in the full spatial distribution of the detected galaxy population, its velocity dispersion distribution, and the combination thereof.

There are two obvious and orthogonal pathways for addressing the above issues. The first is to tie the construction of group catalogues more closely to simulations and to incorporate this calibration process into the mass error estimation for each individual group. The second is to pursue a vigorous programme for deriving improved empirical constraints on the group masses. One obvious starting point is to use the 120 G^3C groups for which 20+ members are known and to undertake further study of these systems via X-ray, radio, strong lensing, and Sunyaev–Zeldovich techniques. Such a project will be critical if we aim to use galaxy groups as truly direct empirical probes of the population of dark matter haloes.

DATA AVAILABILITY

The data underlying this article are available from the GAMA DR4 website, at http://www.gama-survey.org/dr4, or for external data sets via the links provided in the text.

REFERENCES

Alam S. et al., 2015, ApJS, 219, 12
Allen S. W., Evrard A. E., Mantz A. B., 2011, ARA&A, 49, 409
Anderson M. E., Gaspari M., White S. D. M., Wang W., Dai X., 2015, MNRAS, 449, 3806
Asencio E., Banik I., Kroupa P., 2021, MNRAS, 500, 5249
Bahcall N. A., Cen R., 1993, ApJ, 407, L49
Baldry I. K. et al., 2014, MNRAS, 441, 2440
Beers T. C., Flynn K., Gebhardt K., 1990, AJ, 100, 32
Behroozi P. S., Wechsler R. H., Conroy C., 2013, ApJ, 770, 57
Binney J., Tremaine S., 2008, Galactic Dynamics, 2nd edn. Princeton Univ. Press, Princeton, NJ
Böhringer H., Chon G., Collins C. A., 2014, A&A, 570, A31
Böhringer H., Chon G., Collins C. A., Guzzo L., Nowak N., Bobrovskyi S., 2013, A&A, 555, A30
Böhringer H., Chon G., Fukugita M., 2017, A&A, 608, A65
Bond J. R., Cole S., Efstathiou G., Kaiser N., 1991, ApJ, 379, 440

Bower R. G., Benson A. J., Malbon R., Helly J. C., Frenk C. S., Baugh C. M., Cole S., Lacey C. G., 2006, MNRAS, 370, 645

Brainerd T. G., Blandford R. D., Smail I., 1996, ApJ, 466, 623

Brainerd T. G., Villumsen J. V., 1992, ApJ, 394, 409

Brimioulle F., Seitz S., Lerchster M., Bender R., Snigula J., 2013, MNRAS, 432, 1046

Caldwell C. E., McCarthy I. G., Baldry I. K., Collins C. A., Schaye J., Bird S., 2016, MNRAS, 462, 4117

Chauhan G., Lagos C. D. P., Stevens A. R. H., Bravo M., Rhee J., Power C., Obreschkow D., Meyer M., 2021, MNRAS, 506, 4893

Colless M. et al., 2001, MNRAS, 328, 1039

Davies L. J. M. et al., 2018, MNRAS, 480, 768

Dey A. et al., 2019, AJ, 157, 168

Doi M., Fukugita M., Okamura S., Turner E. L., 1995, AJ, 109, 1490

Dong F., Zhang J., Yang X., Zhang J., Luo W., 2019, ApJ, 883, 155

Driver S. P. et al., 2009, Astron. Geophys., 50, 5.12

Driver S. P. et al., 2011, MNRAS, 413, 971

Driver S. P. et al., 2019, The Messenger, 175, 46

Driver S. P. et al., 2022, MNRAS, in press

Driver S. P., Davies L. J., Meyer M., Power C., Robotham A. S. G., Baldry I. K., Liske J., Norberg P., 2016, in Napolitano N. R., Longo G., Marconi M., Paolillo M., Iodice E., eds, The Universe of Digital Sky Surveys, Astrophysics and Space Science Proceedings, Vol. 42. Springer International Publishing, Switzerland, p. 205

Driver S., 2021, Nat. Astron., 5, 852

Duarte M., Mamon G. A., 2014, MNRAS, 440, 1763

Eke V. R. et al., 2004, MNRAS, 348, 866

Eke V. R., Baugh C. M., Cole S., Frenk C. S., Navarro J. F., 2006, MNRAS, 370, 1147

Elahi P. J., Power C., Lagos C. d. P., Poulton R., Robotham A. S. G., 2018, MNRAS, 477, 616

Frenk C. S., White S. D. M., Davis M., Efstathiou G., 1988, ApJ, 327, 507

Han J. et al., 2015, MNRAS, 446, 1356

Hoekstra H., Donahue M., Conselice C. J., McNamara B. R., Voit G. M., 2011, ApJ, 726, 48

Jee M. J., Hughes J. P., Menanteau F., Sifón C., Mandelbaum R., Barrientos L. F., Infante L., Ng K. Y., 2014, ApJ, 785, 20

Jenkins A., Frenk C. S., White S. D. M., Colberg J. M., Cole S., Evrard A. E., Couchman H. M. P., Yoshida N., 2001, MNRAS, 321, 372

Knebe A. et al., 2013, MNRAS, 435, 1618

Kubo J. M., Stebbins A., Annis J., Dell'Antonio I. P., Lin H., Khiabanian H., Frieman J. A., 2007, ApJ, 671, 1466

Lagos C. d. P., Tobar R. J., Robotham A. S. G., Obreschkow D., Mitchell P. D., Power C., Elahi P. J., 2018, MNRAS, 481, 3573

Leauthaud A. et al., 2010, ApJ, 709, 97

Liske J. et al., 2015, MNRAS, 452, 2087

Lukić Z., Heitmann K., Habib S., Bashinsky S., Ricker P. M., 2007, ApJ, 671, 1160

Merson A. I. et al., 2013, MNRAS, 429, 556

Meyer C., 2021, Measuring the Dark Matter Halo Mass Function Using Galaxy Groups. Master's thesis, University of Western Australia

Murray S. G., Diemer B., Chen Z., Neuhold A. G., Schnapp M. A., Peruzzi T., Blevins D., Engelman T., 2021, Astron. Comput., 36, 100487

Murray S. G., Power C., Robotham A. S. G., 2013, MNRAS, 434, L61

Murray S. G., Robotham A. S. G., Power C., 2018, ApJ, 855, 5

Navarro J. F., Frenk C. S., White S. D. M., 1997, ApJ, 490, 493

Old L. et al., 2014, MNRAS, 441, 1513

Old L. et al., 2018, MNRAS, 475, 853

Ondaro-Mallea L., Angulo R. E., Zennaro M., Contreras S., Aricò G., 2021, MNRAS, 509, 6077

Peacock J. A., Heavens A. F., 1990, MNRAS, 243, 133

Planck Collaboration VI, 2020, A&A, 641, A6

Press W. H., Schechter P., 1974, ApJ, 187, 425

Rana D., More S., Miyatake H., Nishimichi T., Takada M., Robotham A. S. G., Hopkins A. M., Holwerda B. W., 2022, MNRAS, 510, 5408

Reed D. S., Bower R., Frenk C. S., Jenkins A., Theuns T., 2007, MNRAS, 374, 2

Reed D., Gardner J., Quinn T., Stadel J., Fardal M., Lake G., Governato F., 2003, MNRAS, 346, 565

Robotham A. S. G. et al., 2011, MNRAS, 416, 2640

Robotham A. S. G., 2016a, Astrophysics Source Code Library, record ascl:1602.011

Robotham A. S. G., 2016b, Astrophysics Source Code Library, record ascl:1604.004

Schechter P., 1976, ApJ, 203, 297

Singari B., Ghosh T., Khatri R., 2020, J. Cosmol. Astropart. Phys., 2020, 028

Sohn J., Geller M. J., Zahid H. J., Fabricant D. G., Diaferio A., Rines K. J., 2017, ApJS, 229, 20

Springel V. et al., 2005, Nature, 435, 629

Stanek R., Evrard A. E., Böhringer H., Schuecker P., Nord B., 2006, ApJ, 648, 956

Strigari L. E., Bullock J. S., Kaplinghat M., Diemand J., Kuhlen M., Madau P., 2007, ApJ, 669, 676

Tempel E. et al., 2014, A&A, 566, A1

Tempel E., Kruuse M., Kipper R., Tuvikene T., Sorce J. G., Stoica R. S., 2018, A&A, 618, A81

Tempel E., Tuvikene T., Kipper R., Libeskind N. I., 2017, A&A, 602, A100

Trevisan M., Mamon G. A., 2017, MNRAS, 471, 2022

Tucker E., Walker M. G., Mateo M., Olszewski E. W., Geringer-Sameth A., Miller C. J., 2020, ApJ, 888, 106

Viola M. et al., 2015, MNRAS, 452, 3529

Watson W. A., Iliev I. T., D'Aloisio A., Knebe A., Shapiro P. R., Yepes G., 2013, MNRAS, 433, 1230

Wechsler R. H., Tinker J. L., 2018, ARA&A, 56, 435

York D. G. et al., 2000, AJ, 120, 1579

Zwicky F., 1933, Helve. Phys. Acta, 6, 110

APPENDIX A

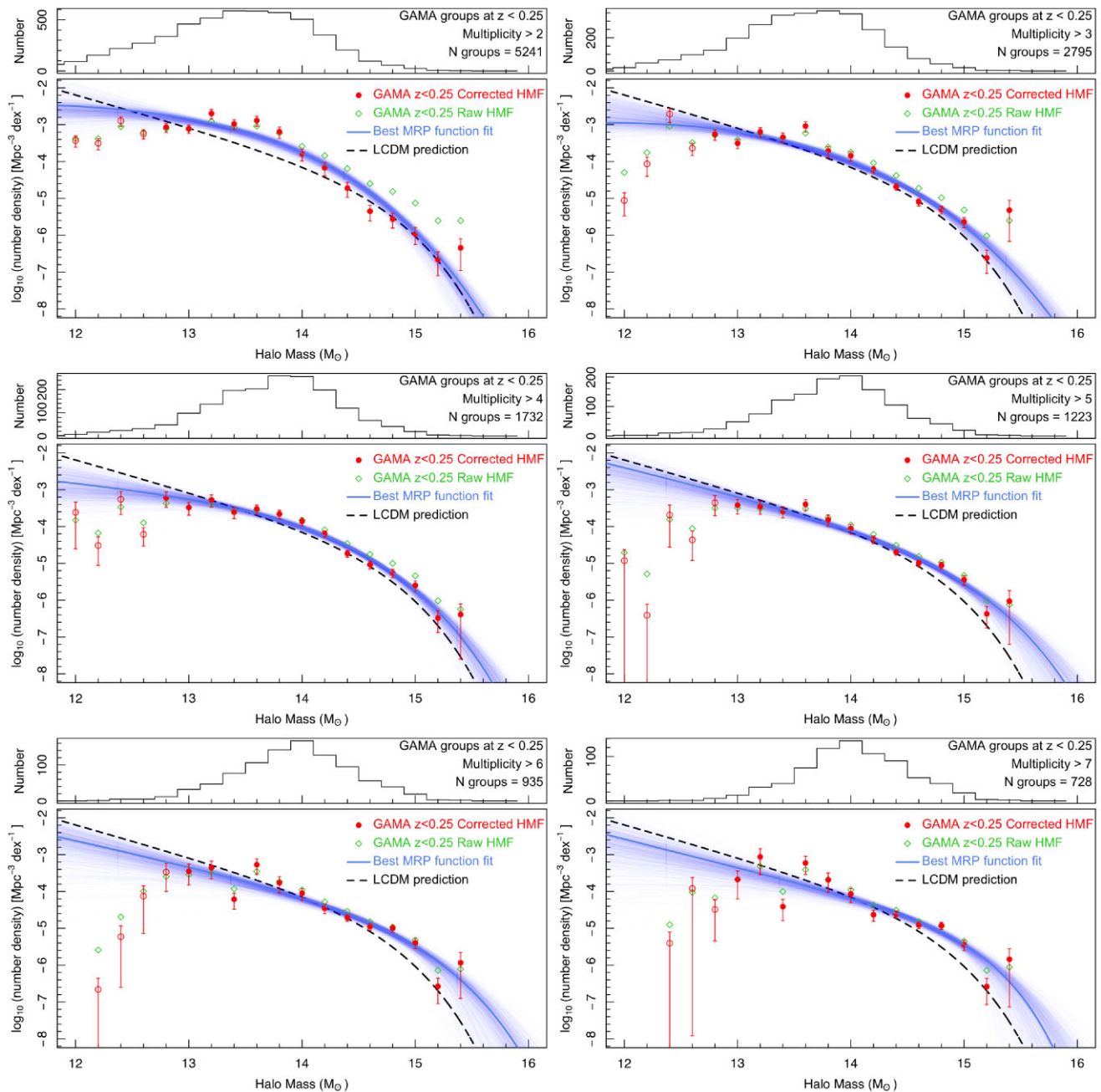All of the HMFs generated in this work are summarized in Fig. 7 and show in Figs. A1, A2, A3 and A4.

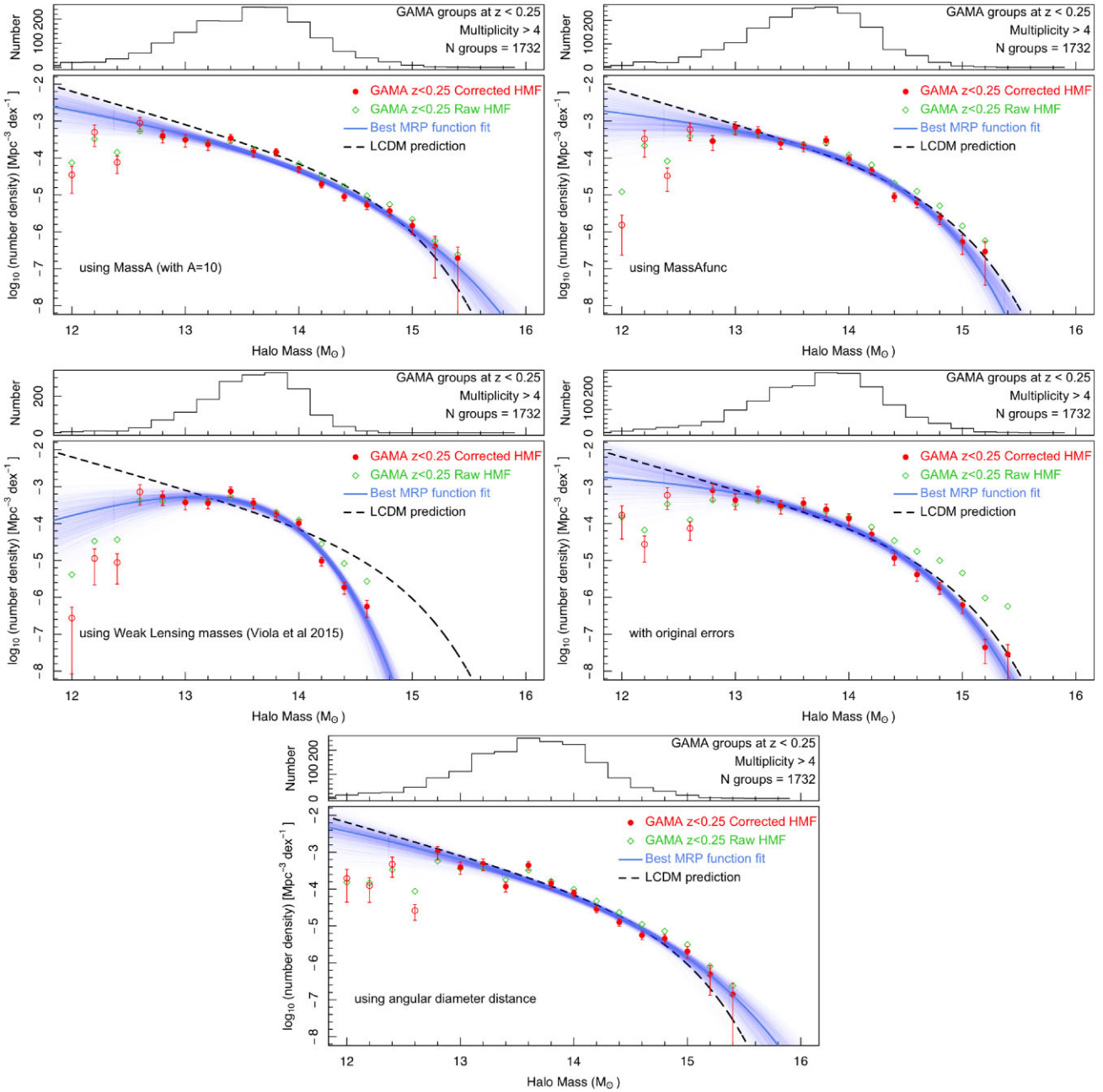**Figure A1.** GAMA HMF derivations for different multiplicity cuts.

Figure A2. GAMA HMF derivations for different mass, error, and distance choices but all with a multiplicity cut of $N_{\rm FoF} > 4$.
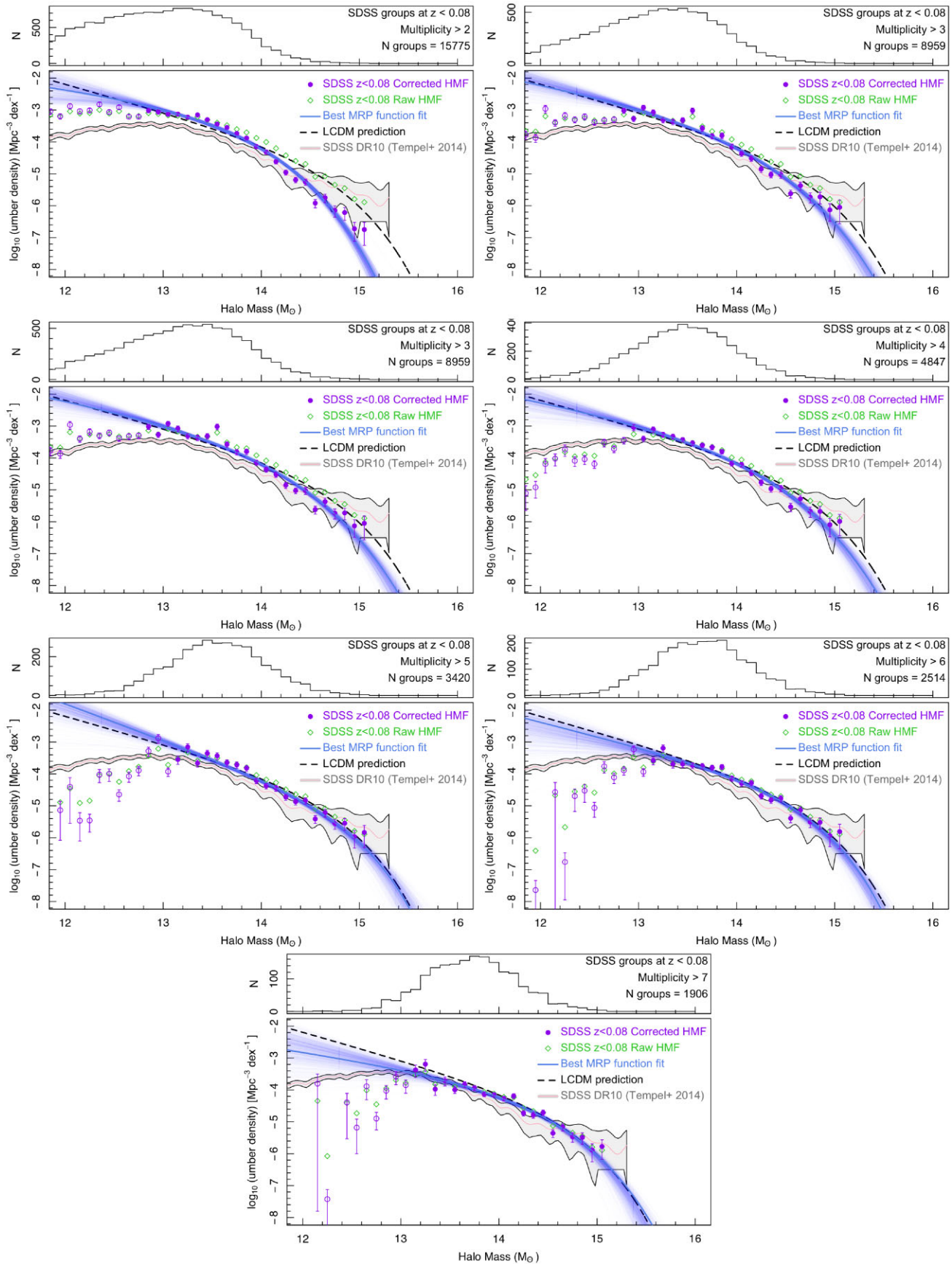
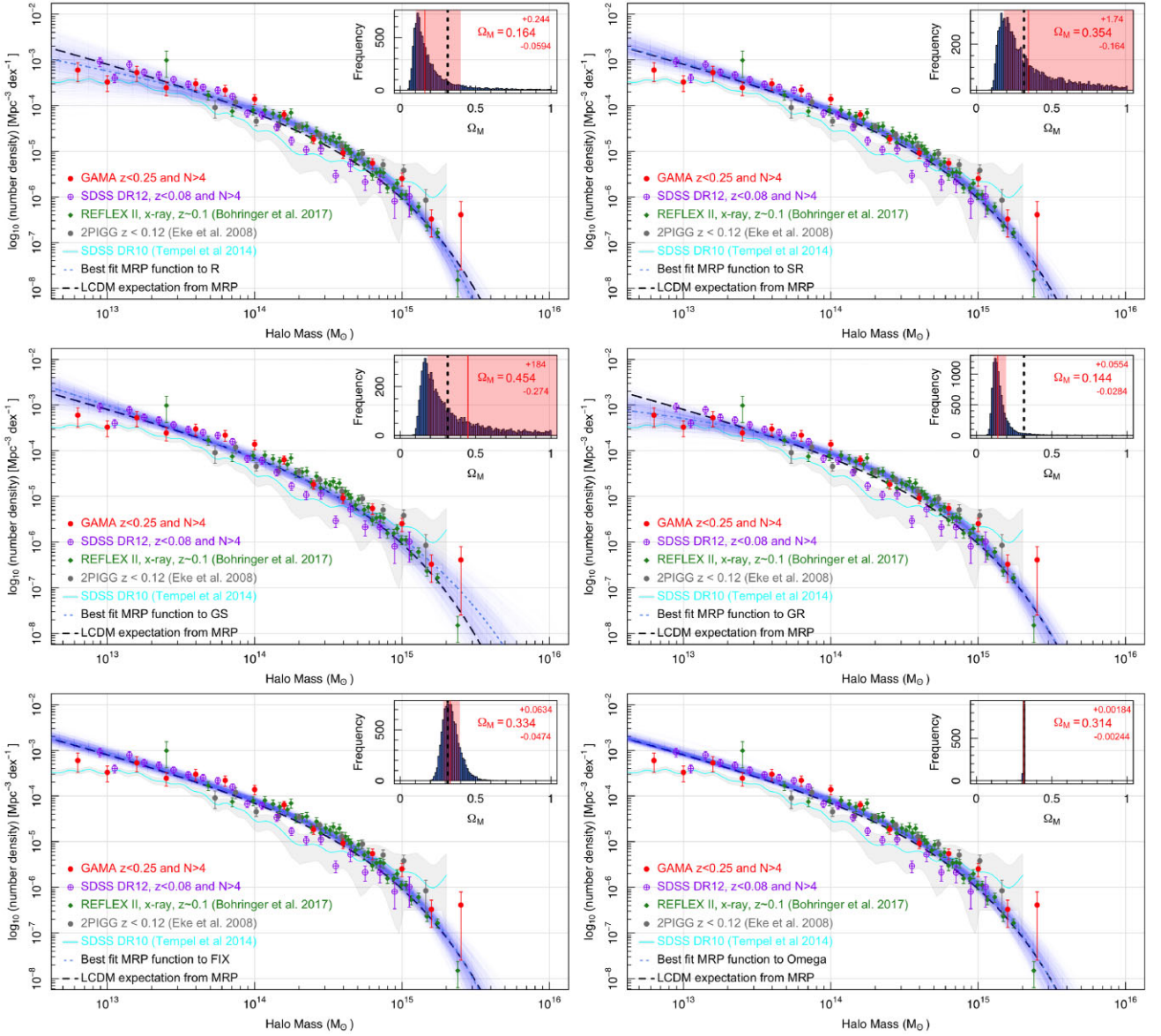**Figure A3.** SDSS HMF derivations for different multiplicity cuts.

Figure A4. Different MRP fits to the GSR data.

This paper has been typeset from a TEX/LATEX file prepared by the author.